~~Poleward shift of the North Pacific storm track driven by springtime~~ Springtime East Asian dust heating contributes to interannual poleward shift of the North Pacific storm track

Anbao Zhu[1, 2, 3], Xin Huang[1, 2], Haiming Xu[3], Jiechun Deng[3], Lian Xue[4], Zilin Wang[1, 2], Ke Ding[1, 2], Tianshuai Li[1, 2], Aijun Ding[1, 2]

[1]Joint International Research Laboratory of Atmospheric and Earth System Sciences, School of Atmospheric Sciences, Nanjing University, Nanjing 210023, China
[2]State Key Laboratory of Severe Weather Meteorological Science and Technology, Nanjing University, Nanjing 210023, China
[3]School of Atmospheric Sciences, Nanjing University of Information Science & Technology, Nanjing 210044, China
[4]Nanjing-Helsinki Institute in Atmospheric and Earth System Sciences, Nanjing University, Suzhou 215163, China

Correspondence to: Xin Huang (xinhuang@nju.edu.cn)

Abstract. The North Pacific storm track plays a key role in shaping climate across ~~shapes precipitation and temperature patterns over~~ the Arctic and western North America by modulating precipitation and temperature, yet ~~how~~ its interannual sensitivity to springtime East Asian dust remains poorly understood. Based on the Modern-Era Retrospective analysis for Research and Applications, Version 2 (MERRA-2) reanalysis data from 1980 to 2022, we find that anomalously high springtime East Asian dust loading is robustly associated with a systematic poleward shift of the North Pacific storm track on interannual timescales. It is revealed that~~The physical mechanism proceeds through a clear causal chain. In details,~~ shortwave absorption by the trans-Pacific dust plume coincides with warming in the ~~warms the mid-troposphere between~~ 850 ~~and~~ 400 hPa layer~~, exciting~~ and an anomalous anticyclonic circulation over the North Pacific. This thermal perturbation restructures the meridional temperature gradient and shifts the zone of maximum Eady growth rate poleward, thereby relocating the preferred region for baroclinic eddy development to higher latitudes. The Weather Research and Forecasting model coupled with Chemistry (WRF-Chem) sensitivity experiments reproduce ~~both~~ the spatial pattern ~~and sign~~ of the storm track response, supporting the proposed radiative–dynamical pathway~~confirming that dust shortwave absorption is sufficient to drive the observed displacement~~. These findings indicate ~~demonstrate~~ that natural dust aerosols can modulate large-scale North Pacific atmospheric dynamics on interannual timescales and suggest that springtime dust variability should be considered in regional climate assessments.

1 Introduction

Storm tracks are regions where extratropical cyclones preferentially form, develop, and dissipate (Shaw et al., 2016). They are largely characterized by transient eddy activities that drive midlatitude atmospheric circulation (Chang et al., 2002). The North Pacific storm track is a major branch of the Northern Hemisphere storm track system. It originates near the East Asian coastal stationary trough (Blackmon, 1976) and is sustained by baroclinic instability that converts mean-flow available potential energy into eddy kinetic energy through the equator-to-pole temperature gradient (Simmons and Hoskins, 1978; Chang et al., 2002). The North Pacific storm track plays a key role in the climate system. It accounts for much of the poleward transport of heat, moisture, and momentum across the North Pacific basin, delivering them into the Arctic and western North America (Trenberth and Stepaniak, 2003; Salathé Jr., 2006). Through this transport, it heavily influences regional weather patterns and midlatitude extreme events, including severe winds and heavy precipitation over both the North Pacific and western North America (Salathé Jr., 2006; Pfahl et al., 2014; Chemke and Yuval, 2026). Spring is particularly important because the North Pacific storm track undergoes its most rapid meridional migration of the annual cycle (Hoskins and Hodges, 2019), and the storm track configuration during this transition governs the frequency of deep stratosphere-to-troposphere mass transport over western North America (Lin et al., 2015; Breeden et al., 2021). Yet springtime storm track variability has nonetheless received far less attention than its wintertime counterpart. Therefore, it is essential to understand its variability, particularly in spring, for regional weather forecasting and climate prediction (Shaw et al., 2016).

East Asia is one of the world's major source regions of mineral dust aerosols (Kok et al., 2023). Every spring, ~~intense~~ dust plumes originate from the Taklimakan and Gobi Deserts and are transported eastward by mid-latitude westerlies, forming an extensive aerosol belt over the North Pacific (Huang et al., 2014; Yu et al., 2019). Dust accounts for more than 50% of the total aerosol column mass over the North Pacific in spring, the highest fraction among the four seasons (Hu et al., 2019). Unlike predominantly scattering aerosols, mineral dust exhibits substantial shortwave absorption due to its iron oxide content (Sokolik and Toon, 1999), producing notable radiative heating within the atmospheric column (Chen et al., 2017). This ~~dust~~ radiative heating ~~can significantly~~ modulates large-scale atmospheric circulation~~,~~ and weather systems, with documented effects on ~~and air pollution, such as~~ the Indian summer monsoon (Lau et al., 2006; Jin et al., 2021) ~~(Lau and Kim and Kim, 2006; Jin et al., 2021)~~, Atlantic hurricanes (Sun and Zhao, 2020; Xian et al., 2020), Mongolian cyclones (Chen et al., 2023), and ~~P~~particle and ~~O~~ozone ~~P~~pollution in East China (Wang et al., 2020). Observational records also show a recent increase in severe dust storms over East Asia (Yin et al., 2022; Yin et al., 2026), leading to substantial perturbations on radiative energy balance (Gui et al., 2022). The increasing frequency of these extreme events underscores the need to evaluate the climatic impacts of springtime dust variability.

Although the influence of aerosols on the North Pacific storm track has received increasing attention, most previous studies have focused on wintertime anthropogenic aerosols. Modelling studies demonstrate that East Asian anthropogenic emissions

induce an equatorward shift of the subtropical jet and the North Pacific storm track in boreal winter, primarily by cooling the surface through aerosol–radiation interactions (Ming et al., 2011; Zhou and Deng, 2013; Wang et al., 2015; Liu et al., 2019)~~(Ming and Ramaswamy and Chen, 2011; Zhou and Deng, 2013; Wang and Jiang and Su, 2015; Liu et al., 2019)~~. Furthermore, through aerosol–cloud interactions, anthropogenic aerosols that act as cloud condensation nuclei enhance deep convective clouds and intensify mid-latitude cyclones, resulting in approximately 7% more precipitation within the wintertime Pacific storm track (Zhang et al., 2007; Wang et al., 2014a, b)~~(Zhang et al., 2007; Wang and Zhang and Saravanan, 2014; Wang et al., 2014)~~. However, during spring, when the East Asian–North Pacific aerosol regime transitions from anthropogenic-dominated to dust-dominated (Zhu et al., 2007; Bao et al., 2009)~~(Zhu et al., 2007; Bao and Wen and Wu, 2009)~~, the storm track response to springtime dust remains largely unexplored. Notably, satellite-based analyses reveal that wintertime East Asian aerosols significantly enhance deep convective clouds in the North Pacific storm track. Interestingly, this signal disappears in spring, even though the aerosol optical depth (AOD) reaches its annual maximum during this season (Bender et al., 2012) ~~(Bender and Ramanathan and Tselioudis, 2012)~~. This seasonal contrast suggests that springtime dust aerosols may exert fundamentally different effects on the storm track compared to wintertime anthropogenic aerosols. Moreover, previous assessments of aerosol effects on the North Pacific storm track have largely addressed the response to long-term emission changes, whereas the response to year-to-year aerosol variability remains unclear.

This study investigates the interannual impact of springtime East Asian dust aerosols on the North Pacific storm track by using reanalysis data from 1980 to 2022, along with modelling sensitivity experiments. Specifically, this research aims to determine how East Asian dust aerosols affect the North Pacific storm track during spring on an interannual timescale and to identify the underlying physical mechanisms. The remainder of the paper is organized as follows. Section 2 describes the data and methodology. Section 3 presents the observational evidence and physical mechanisms, which are further verified by modelling simulations. Finally, Section 4 discusses the implications and limitations~~provides the conclusions and discussion~~.

2 Methodology

2.1 Data

The primary dataset used in this study is the Modern Era Retrospective analysis for Research and Applications, Version 2 (MERRA-2). It is provided by the National Aeronautics and Space Administration Global Modeling and Assimilation Office (GMAO) (Gelaro et al., 2017). We utilize MERRA-2 for both aerosol and meteorological fields to ensure dynamic consistency. The data are provided on a 0.5° by 0.65° spatial grid with 72 vertical levels. The MERRA-2 aerosol data are generated using the Goddard Chemistry Aerosol Radiation and Transport (GOCART) model coupled with the Goddard Earth Observing System (GEOS-5) data assimilation system. The GOCART model simulates five aerosol species: dust, black carbon, organic carbon, sulfate, and sea salt. Furthermore, GEOS-5 assimilates bias-corrected AOD from various observation platforms. These include the Advanced Very High Resolution Radiometer (AVHRR) instrument over oceans (Heidinger et al., 2014), the

Moderate Resolution Imaging Spectroradiometer (MODIS) instrument from Terra and Aqua satellites (Levy et al., 2010), the Multiangle Imaging Spectroradiometer (MISR)~~MISR~~ instrument over desert regions (Kahn et al., 2005), and ground-based AERONET stations (Holben et al., 1998).

We use the monthly mean dust column mass density from MERRA-2 to represent the atmospheric dust loading over East Asia and the North Pacific. Recent evaluations indicate that MERRA-2 slightly underestimates absolute dust concentrations compared to ground-based retrievals. However, it exhibits a high temporal correlation with station observations (Zhang et al., 2024). Because MERRA-2 accurately captures the spatiotemporal variability of dust aerosols, this product is widely used in climate analyses (Wang et al., 2021; Li et al., 2023; Fu et al., 2026)~~(Wang and Lau and Wang, 2021; Li et al., 2023; Fu et al., 2026)~~. We also use the AOD from the 1° MODIS Terra Level-3 monthly product (MOD08_M3) (Gupta et al., 2016) to evaluate the model's simulation of dust aerosol spatial distribution. Alongside the aerosol data, we utilize MERRA-2 atmospheric variables, including geopotential height, air temperature, vertical velocity, and horizontal winds. Additionally, we obtain monthly precipitation data on a 2.5° by 2.5° grid from the Climate Prediction Center Merged Analysis of Precipitation (CMAP) dataset (Xie and Arkin, 1997). We also use the satellite-vegetation-based estimate of East Asian spring dust emission from Fu et al. (2026) as an independent dust metric. It is derived from Global Inventory Modeling and Mapping Studies (GIMMS; 1982–2015) and MODIS (2001–2023) vegetation products, which agree closely over their overlap period. Regressions onto this emission index are performed for 1982–2022, the period covered by both datasets. Both the spring North Atlantic Oscillation (NAO) index and the preceding-winter (December to February) Oceanic Niño Index (ONI) are obtained from the National Oceanic and Atmospheric Administration (NOAA) Climate Prediction Center.

2.2 Storm track definition and statistical methods

We define storm track activity using two metrics. The first is the upper-tropospheric transient eddy geopotential height variance at 300 hPa ($Z'Z'_{300}$). The second is the lower-tropospheric transient eddy meridional heat flux at 850 hPa ($V'T'_{850}$). Together, these two metrics provide a comprehensive three-dimensional representation of storm track activity (Chang et al., 2002)~~(Chang and Lee and Swanson, 2002)~~. We calculate the transient variance and heat flux using daily MERRA-2 data. A 2.5–6-day bandpass filter is applied to these daily data to isolate synoptic-scale fluctuations. To quantify atmospheric baroclinicity, we compute the maximum Eady growth rate (EGR) defined as:

$$\sigma_{EGR} = 0.31 \frac{f}{N} \left|\frac{\partial U}{\partial z}\right|,$$

where f is the Coriolis parameter, N is the Brunt-Väisälä frequency, and $\left|\frac{\partial U}{\partial z}\right|$ is the vertical ~~wind~~ shear of the zonal wind (Lindzen and Farrell, 1980). Both N and the vertical wind shear are calculated from daily MERRA-2 data using finite differences between adjacent pressure levels, based on 17 levels from 1000 to 100 hPa (1000, 950, 900, 850, 800, 750, 700, 650, 600, 550, 500, 450, 400, 350, 300, 200 and 100 hPa).

The MERRA-2 and CMAP data~~All datasets used in this study~~ span the period from 1980 to 2022. $Z'Z'_{300}$, $V'T'_{850}$ and EGR are first calculated from daily data and then averaged over spring (March to May). All other variables are obtained by averaging monthly means over spring. This yields one value per year for every variable. To isolate interannual variability, Fourier analysis is applied at each grid point to these spring-mean time series. The first four harmonics, which represent fluctuations with periods longer than about 10 years, are defined as the interdecadal component. The residual after removing the time mean and these harmonics is defined as the interannual component ~~we apply Fourier analysis to remove the first four harmonics from the time series. This procedure effectively filters out interdecadal background signals~~ (Awan and Bae, 2016; Zhu et al., 2021). All quantities analysed below refer to interannual anomalies unless otherwise stated. Regressions throughout this study are performed against a dust index that has been normalized by its own standard deviation. Specifically, for a dust index $\boldsymbol{D}$ with interannual standard deviation $\boldsymbol{\sigma_D}$ and standardized form $\boldsymbol{D} = \frac{\boldsymbol{D}}{\boldsymbol{\sigma_D}}$, the regression coefficient of an interannual anomaly field $\boldsymbol{Y}$ is obtained as the least-squares slope

$$\boldsymbol{\beta} = \frac{\sum_t \boldsymbol{Y}_t \widehat{\boldsymbol{D}}_t}{\sum_t \widehat{\boldsymbol{D}}_t^2}.$$

Because $\widehat{\boldsymbol{D}}$ is dimensionless, $\boldsymbol{\beta}$ retains the physical unit of $\boldsymbol{Y}$ and represents the response of $\boldsymbol{Y}$ to a one-standard-deviation increase of the dust index.

On interannual timescales, the variability of the North Pacific storm track is closely linked to the El Niño Southern Oscillation (ENSO). During El Niño events, the Pacific storm track typically shifts equatorward and extends downstream (Seager et al., 2010; Jiang et al., 2013) ~~(Seager et al., 2010; Jiang and Deng and Li, 2013)~~. To remove the ENSO-driven circulation signal before examining the dust effect, we employ partial regression methods~~To explicitly isolate the physical impacts of dust aerosols from these ENSO-driven circulation changes, we employ partial regression methods~~ (Cai et al., 2011; Liguori et al., 2022). Specifically, we use the ONI averaged over the preceding winter (December to February), when ENSO typically peaks, as the ENSO indicator and linearly regress out its signal from all variables before regressing the storm track fields onto the dust index~~Specifically, we use the Niño 3.4 index as the ENSO indicator and linearly regress out its concurrent spring signal from all variables prior to the dust-storm track regression analysis~~. Furthermore, we use empirical orthogonal function (EOF) analysis to extract dominant variability patterns. Finally, the statistical significance of all correlation and regression results is evaluated using a two-tailed Student's *t*-test.

2.3 Model configuration and experimental design

We use the Weather Research and Forecasting model coupled with Chemistry (WRF-Chem) version 3.9.1. This model simulates meteorological processes and dust activities over East Asia and the North Pacific during the boreal spring. The simulation domain spans from East Asia to the central North Pacific. It employs a regular latitude and longitude projection with 381 by 131 grid points centred at 50°N and 160°E (Figure S1). The horizontal resolution is 0.5° by 0.5°, which

corresponds to approximately 55 km. The vertical grid contains 45 levels extending from the surface up to 50 hPa. Initial and boundary meteorological conditions are derived from the National Centres for Environmental Prediction (NCEP) Final Analysis (FNL) data (NCEP, 2000)(Ncep, 2000). These data have a 1° spatial resolution and update every 6 hours. Additionally, we incorporate sea surface temperature data from the NCEP real time global sea surface temperature analysis.

We configure the model with a comprehensive suite of physical and chemical parameterization schemes. Table 1 summarizes these specific options. For cloud and precipitation processes, we select the Lin microphysics scheme (Chen and SunLin and Colle, 20021) and the Grell-3D ensemble cumulus scheme (Grell, 1993; Grell and Dévényi, 2002). The Rapid Radiative Transfer Model for General Circulation Models (RRTMG) calculates both shortwave and longwave radiation while accounting for aerosol radiative effects (Iacono et al., 2008). Planetary boundary layer processes are parameterized using the Yonsei University (YSU) scheme (Hong et al., 2006)(Hong and Noh and Dudhia, 2006). This is coupled with the MM5 Monin-Obukhov surface layer scheme and the Unified Noah land surface model to represent surface physics and land atmosphere interactions (Pahlow et al., 2001; Chen et al., 2010)(Pahlow and Parlange and Porté-Agel, 2001; Chen et al., 2010). For atmospheric chemistry, we employ the second--generation Regional Acid Deposition Model (RADM2) for gas phase reactions (Stockwell et al., 1990), alongside the Fast-J photolysis scheme. The GOCART module simulates aerosol chemistry (Chin et al., 2002). Aerosol optical properties are computed using the Maxwell Garnett approximation (Bohren and Huffman, 1983). Finally, we adopt the Shao 2004 dust emission scheme (Shao, 2004). Previous studies demonstrate its excellent performance in simulating dust emissions and the spatiotemporal variability of dust mass concentrations over East Asia (Tang et al., 2018; Zhao et al., 2020; Idrissa et al., 2024).

Table 1. Physical and chemical parameterizations used in WRF-Chem modeling parameterization option settings

Option name	Scheme
Longwave radiation	RRTMG
Shortwave radiation	RRTMG
Microphysics	Lin
Boundary layer	YSU
Cumulus	Grell-3D
Land surface	Unified Noah
Surface layer	MM5 Monin-Obukhov
Aerosol chemistry	GOCART
Gas chemistry	RADM2
Photolysis	Fast-J
Dust emissions	Shao2004

We design two sets of simulations to test whether dust radiative heating alone can reproduce the physical pathway inferred from the reanalysis~~investigate the radiative and dynamical impacts of dust aerosols on the North Pacific storm track~~. The control experiment (CTRL) incorporates full dust emissions. In contrast, the sensitivity experiment (NoDust) completely disables dust emissions. We attribute the atmospheric differences between the CTRL and NoDust simulations directly to the effects of dust aerosols. We select the year 2018 as our study period because the East Asian dust loading during this year significantly exceeded the climatological mean (Figure 2b). To enhance the statistical robustness of our results, we conduct seven ensemble members for each experiment. These ensemble members are initialized one day apart from 19 to 25 February 2018. All simulations conclude on 31 May 2018. We treat February as the model spin-up period and exclude it from the final analysis. Consequently, our analysis focuses strictly on the boreal spring season from March to May 2018. Because the experiments cover a single spring, they cannot reproduce the interannual relationship diagnosed from the reanalysis or determine whether dust is its dominant cause. They are instead designed as a process-level verification of the proposed mechanism. Since the two experiments share identical meteorological initial and boundary conditions, their difference isolates the dust effect from concurrent circulation variability~~We acknowledge that this single-year simulation cannot fully capture the interannual variability present in the reanalysis. The WRF-Chem experiments are therefore designed as a process-level verification of the proposed physical mechanism rather than as an independent confirmation of the interannual statistical relationship~~.

As an additional and indirect check, we also perform a pair of Community Earth System Model 2 (CESM2.1) experiments in the F2000climo configuration (Danabasogluet al., 2020), with and without dust emission (one member each). Both runs are integrated from January to May with boundary conditions representative of the 1995–2005 mean, and the first two months are discarded as spin-up. These experiments are not designed to quantify the dust effect. They serve only to illustrate how much the magnitude of the simulated response differs between models.

3 Results

3.1 ~~Observational~~ Observed association ~~link~~ between East Asian dust and the North Pacific storm track

As shown in Figure 1, Asian dust loading peaks over the Taklimakan and Gobi deserts and extends eastward over the North Pacific, spatially overlapping with the storm track region, characterized by $Z'Z'_{300}$ (red contours) and $V'T'_{850}$ (orange contours). This spatial collocation suggests the potential for dynamical interactions between dust aerosols and storm track activity, motivating the present investigation. To further characterize the spatiotemporal variability of East Asian dust loading, we apply EOF analysis to the spring dust column mass density anomalies over 1980–2022, with spring defined as March–April–May (MAM). The leading EOF mode (EOF1; Figure 2a) explains approximately 46% of the total variance and is characterized by same-sign loading across East Asia, with the largest amplitude over the Taklimakan and Gobi deserts. This

pattern is consistent with the known structure of dust variability, in which the most pronounced fluctuations are concentrated over the major source regions (Guo et al., 2019).

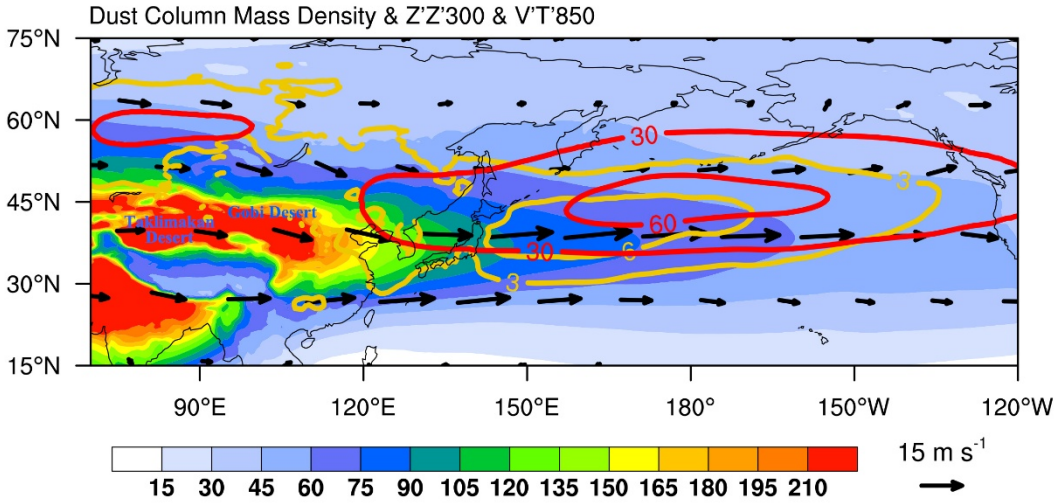


Figure 1. Spatial distribution of climatological spring (March-April-May, MAM) mean dust column mass density (shading; mg m^{-2}), 500 hPa wind (vector; m s^{-1}), transient eddy meridional heat flux at 850 hPa ($\overline{V'T'}_{850}$, EMHF; orange contour with interval of 3 K m s^{-1}) and transient variances of geopotential height at 300 hPa ($\overline{Z'Z'}_{300}$, EGHV ; red contour with interval of 30 dagpm^2) averaged over 1980–2022.

Based on this spatial pattern, we define an East Asian dust index (EADI) as the area-averaged dust column mass density over the key region (35°–47°N, 76°–118°E; black box in Figure 2a) where the variance is largest. The resulting EADI is highly correlated with the EOF1 principal component (PC1), with a correlation coefficient exceeding 0.97 (Figure 2b), confirming that the EADI effectively captures both interannual and interdecadal variability of spring East Asian dust loading. The temporal evolution of EADI reveals two distinct timescales of variability. On the interdecadal timescale, an abrupt increase occurs around 1999, coinciding with a phase reversal in PC1 from negative to positive, which has been linked to changes in 10-m wind speed over dust source regions (Guo et al., 2019). On the interannual timescale, the EADI exhibits substantial year-to-year fluctuations, reflecting the large variability in dust emission and transport processes (Yu et al., 2019). Given that interannual variability constitutes an important component of total dust variability, this study focuses on the North Pacific storm track response to the interannual dust variability over East Asia. The interdecadal component is therefore removed (Section 2.2), so that the storm track response discussed below reflects year-to-year dust variations rather than the long-term change in dust loading~~Unless otherwise stated, all variables discussed hereafter refer to their interannual components~~.

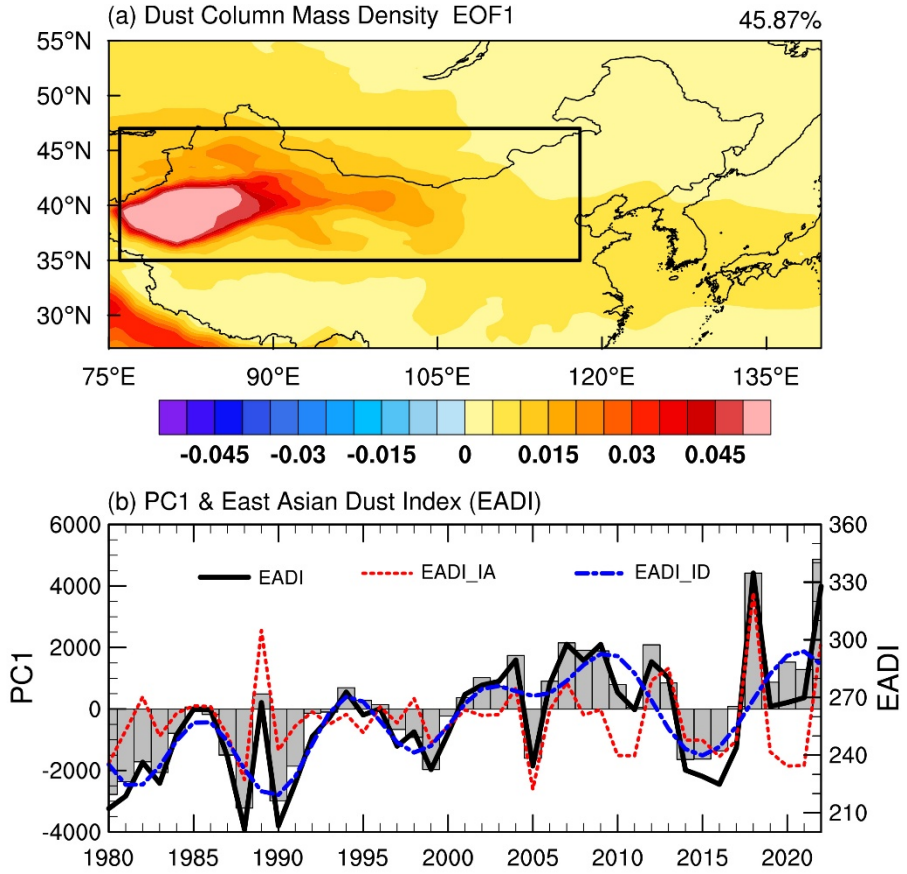
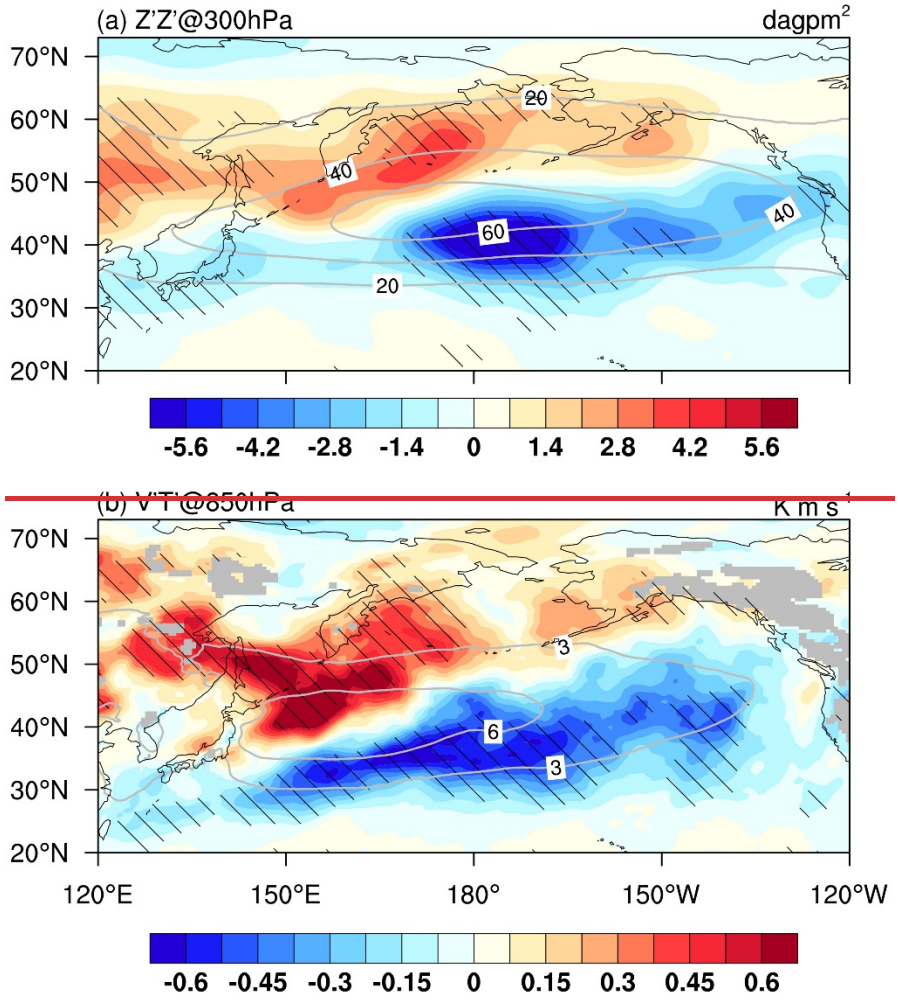


Figure 2. (a) Spatial pattern (shading) and (b) principal component (gray bars) of the first EOF mode of MAM mean dust column mass density over East Asia during 1980–2022. The spring East Asian dust index (EADI; black solid line) defined as dust column mass density averaged over East Asia [76°–118°E, 35°–47°N; the black box in (a)] is also plotted in (b), together with its interannual component (EADI_IA; red dashed line) and interdecadal component (EADI_ID; blue dashed line). The interdecadal component is the sum of the first four Fourier harmonics (periods longer than about 10 years), and the interannual component is the residual.

To investigate the interannual relationship between East Asian dust loading and the North Pacific storm track, Figure 3 presents the regression of anomalous $Z'Z'_{300}$ and $V'T'_{850}$ onto the interannual component of the EADI. Both fields exhibit a meridional dipole pattern that is approximately symmetric about the climatological storm track axis, suggesting a systematic poleward displacement of storm track activity during high-dust springs (relative to low-dust springs). Specifically, significant negative $Z'Z'_{300}$ anomalies appear over the East China Sea and the east-central North Pacific, with the largest reduction reaching approximately 7.5 dagpm^2 (~15% of the climatological mean). Meanwhile, significant positive anomalies exceeding 2.0 dagpm2 (more than 8% of the climatological mean) emerge over eastern Siberia and the Bering Sea (Figure 3a). A similar dipole structure is evident in $V'T'_{850}$: negative anomalies extend zonally along the southern flank of the climatological heat flux maximum, with the reduction more pronounced over the downstream region of the storm track. Concurrently, prominent positive anomalies cover eastern Siberia, the Kamchatka Peninsula, and Alaska (Figure 3b)~~, indicating enhanced poleward eddy heat transport driven by East Asian dust outflow~~. These results suggest that increased springtime East Asian dust loading

is associated with a poleward shift of both the North Pacific storm track and its ~~a strengthening of poleward~~ transient meridional ~~eddy~~ heat transport on interannual timescales. The precipitation response corroborates this poleward shift, with reduced rainfall along the southern flank and a slight enhancement near the Bering Sea (Figure S2).


(a) Z'Z'@300hPa
dagpm^2
70°N
60°N
50°N
40°N
30°N
20°N
20
40
60
40
20
-5.6 -4.2 -2.8 -1.4 0 1.4 2.8 4.2 5.6
(b) V'T'@850hPa
K m s^{-1}
70°N
60°N
50°N
40°N
30°N
20°N
3
6
3
120°E
150°E
180°
150°W
120°W
-0.6 -0.45 -0.3 -0.15 0 0.15 0.3 0.45 0.6

248

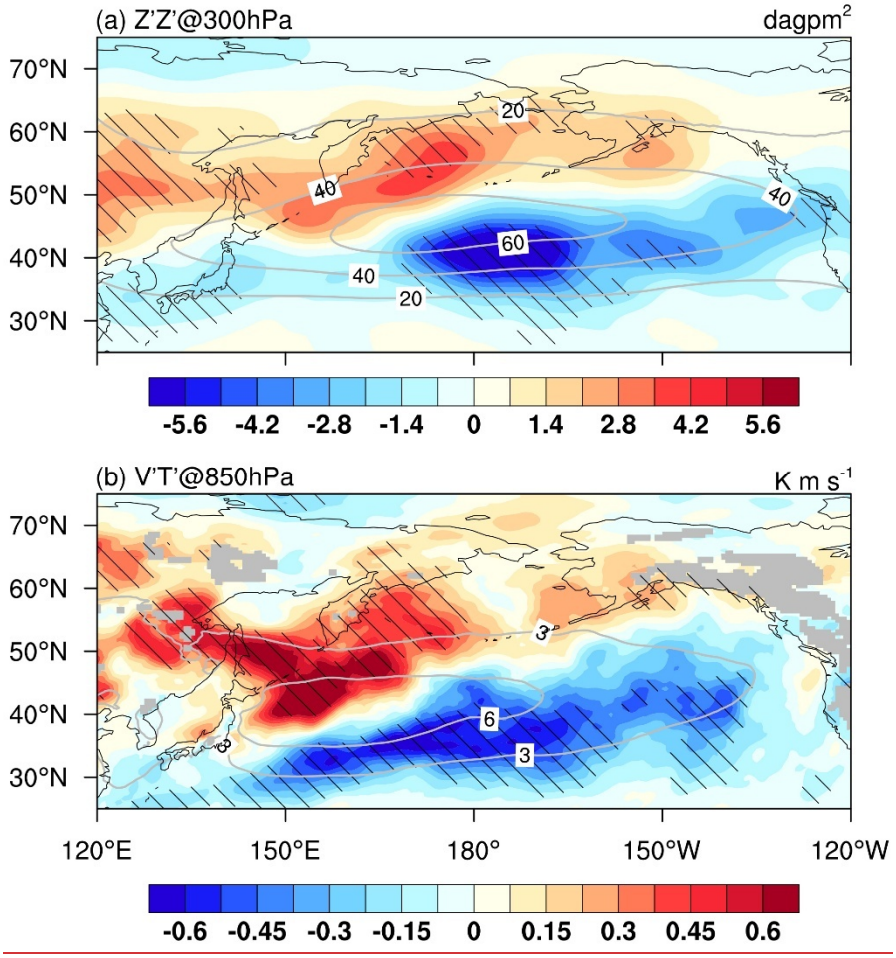


Figure 3. Regressions of anomalies in (a) transient variances of 300 hPa geopotential height ($Z'Z'_{300}$; shading; dagpm^2) and (b) 850 hPa transient eddy meridional heat flux ($V'T'_{850}$; shading; K m s^{-1}) onto the standardized EADI_IA; the shading therefore gives the response per one standard deviation of EADI_IA. Grey contours denote the climatological spring mean of (a) $Z'Z'_{300}$ and (b) $V'T'_{850}$. Hatching denotes the anomalies statistically significant at the 95% confidence level based on the Student's *t* test.

To further quantify this relationship, we define storm track position indices as the difference in area-averaged $Z'Z'_{300}$ and $V'T'_{850}$ between a northern box and a southern box on the poleward and equatorward flanks of the climatological storm track (Figures S3a-b). Positive indices therefore denote a poleward displacement of the storm track. Both position indices covary with the interannual variations of the EADI and dust PC1 (Figure S3c), with correlation coefficients ranging from 0.36 to 0.47, all significant at the 95% confidence level. The EADI alone explains about 22% and 15% of the interannual variance in the $Z'Z'_{300}$ and $V'T'_{850}$ position indices, respectively. The remaining variance likely reflects internal atmospheric variability and other drivers, including large-scale circulation anomalies that may influence both dust emission and the storm track.

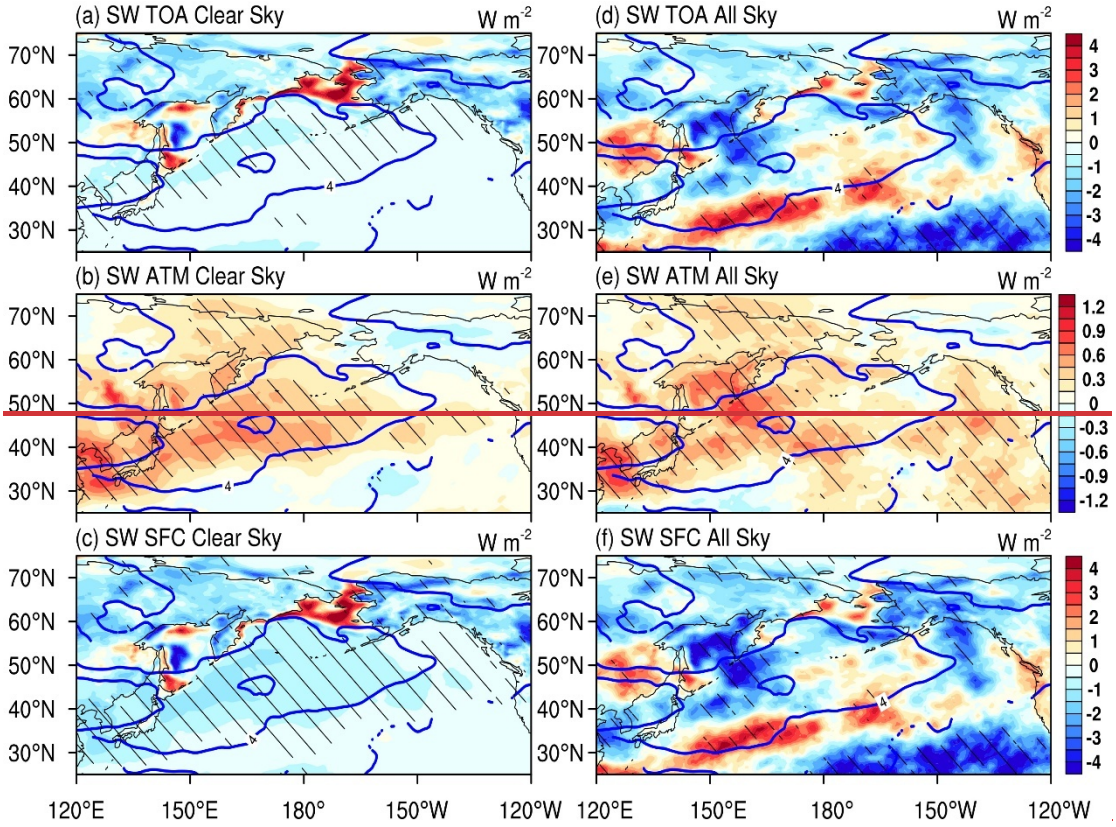
The relationship is robust to the choice of dust index and to the removal of other circulation modes. The dipole in Figure 3 is essentially unchanged when the concurrent spring NAO signal is removed in addition to ENSO (Figure S4). Regressing the

storm track metrics onto the independent emission estimate of Fu et al. (2026) reproduces the same dipole with the same sign and location (Figure S5). Because dust emission is governed mainly by source-region surface wind and land surface conditions, this agreement suggests that the storm track signal is not simply an artefact of the circulation that transports dust across the Pacific. Source-region wind is nevertheless related to the large-scale circulation, so a common driver cannot be fully excluded with reanalysis data alone.

3.2 Possible ~~physical~~ radiative–dynamical mechanism ~~underlying the~~linking dust aerosol~~–~~ and the storm tracks ~~relationship~~

Having established the statistical association between East Asian dust loading and the poleward shift of the North Pacific storm track, we then examine the possible underlying physical mechanisms. ~~Given d~~Dust aerosols perturb the radiative energy balance ~~through~~by scattering and absorbing solar radiation, which redistributes~~thereby redistributing~~ radiative energy~~,~~ and ~~modifying~~ can modify the large-scale circulation~~,~~. ~~we~~ We therefore first examine the shortwave (SW) ~~r~~absorption within the atmospheric column~~adiative flux anomalies~~ associated with East Asian dust loading (Figure 4). Under clear-sky conditions ~~(Figure 4a–c)~~, absorption by mineral dust increases the SW energy retained in the atmosphere by 0.3–0.6 W m^{-2} over the dust polluted region (Figure 4a), directly ~~dust aerosols transported over the North Pacific backscatters a fraction of incoming solar radiation, reducing the net downward SW flux at the top of the atmosphere (TOA) by approximately 1 W m^{-2} over the dust polluted region (Figure 4a). Simultaneously, absorption of solar radiation by mineral dust induces a significant positive radiative forcing of 0.3–0.6 W m^{-2} in the atmosphere (Figure 4b), leading to direct~~ heating the atmospheric column. The absorption is stronger under all-sky conditions (Figure 4b). When dust resides above cloud layers, the underlying clouds act as a bright reflective surface that enhances multiple scattering between the aerosol and cloud layers and thereby amplifies the atmospheric absorption, consistent with the satellite-based analysis of Xu et al. (2017). These magnitudes are broadly consistent with previous estimates over the North Pacific (Zhu et al., 2007; Hu et al., 2019). The corresponding SW flux changes at the top of the atmosphere and at the surface are shown in Figure S6. Their all-sky minus clear-sky differences exhibit a meridional dipole that mainly reflects the cloud redistribution accompanying the storm track shift, and they are therefore not used here to identify the thermal driver.

~~The combined effects of scattering and atmospheric absorption generate a pronounced dimming effect at the ground surface, reducing the net SW flux by 1.0–1.5 W m^{-2} over regions with high dust loading (Figure 4c). These magnitudes of dust-induced SW radiative perturbations are broadly consistent with previous estimates over the North Pacific.~~


(a) SW TOA Clear Sky
W m-2
(d) SW TOA All Sky
W m-2
(b) SW ATM Clear Sky
W m-2
(e) SW ATM All Sky
W m-2
(c) SW SFC Clear Sky
W m-2
(f) SW SFC All Sky
W m-2
70°N
60°N
50°N
40°N
30°N
120°E
150°E
180°
150°W
120°W
4
3
2
1
0
-1
-2
-3
-4
1.2
0.9
0.6
0.3
0
-0.3
-0.6
-0.9
-1.2

291

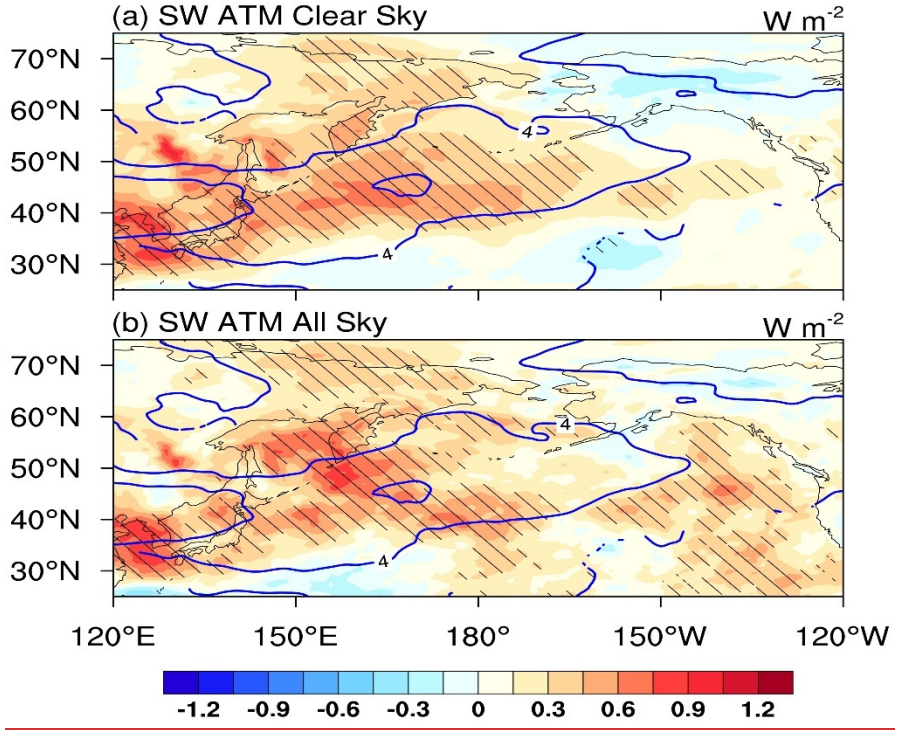
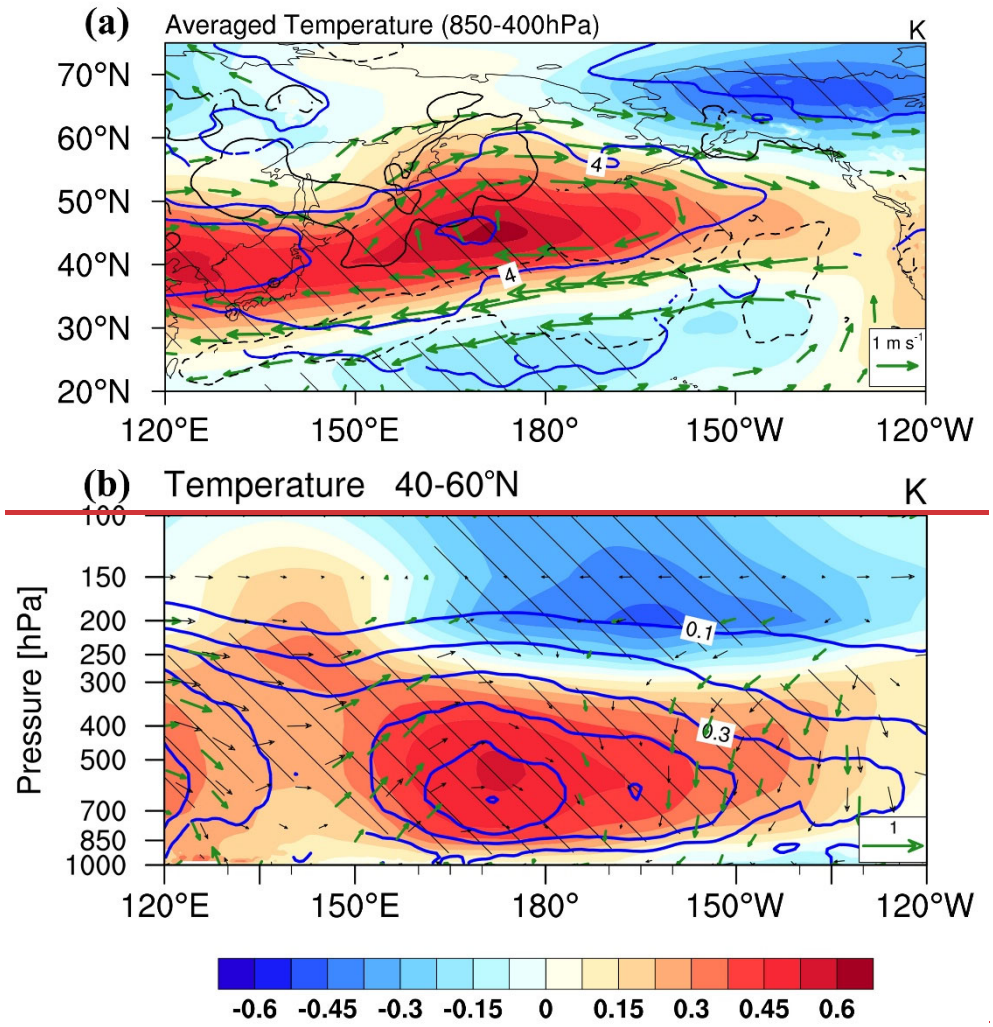


Figure 4. Regressions of anomalies in shortwave radiative fluxes (shading; W m^{-2}) ~~at (a, d) the top of the atmosphere (TOA), (b, e) in the atmosphere (ATM), and (c, f) at the surface (SFC)~~ and dust column mass density (blue contour with interval of 2 mg m^{-2}) onto the standardized EADI_IA for (a) clear-sky conditions and (b) all-sky conditions. The regressed fields therefore give the response per one standard deviation of EADI_IA. Positive values denote increased SW absorption within the atmospheric column~~The left column (a, b, c) represents clear-sky conditions, and the right column (d, e, f) represents all-sky conditions. Downward radiation is defined as positive at the TOA and the SFC; therefore, positive (negative) value means absorb/warming (irradiate/cooling) effects in the ATM~~. Hatching indicates that the regressed anomalies in shortwave radiative fluxes are statistically significant at the 95 % confidence level based on a Student's *t* test.

~~Under all-sky conditions (Figure 4d–f), cloud cover substantially modulates these radiative effects. Over the Sea of Okhotsk and the region south of the Kuril Islands, increased cloudiness (consistent with the enhanced precipitation shown in Figure S2) reflects additional solar radiation, amplifying the negative TOA forcing relative to clear-sky conditions (Figure 4d). Furthermore, when dust resides above cloud layers, the underlying clouds provide as a bright reflective surface that enhances the multiple scattering between the aerosol and cloud layers, thereby amplifying both the atmospheric absorption and the surface cooling effects (Figure 4e–f). This amplification phenomenon is consistent with the satellite-based analysis of Xu et al. (2017).~~

The enhanced shortwave absorption documented above is expected to warm the mid-troposphere and subsequently modify the large-scale circulation. Figure 5a shows the 850–400 hPa averaged temperature and 500 hPa wind anomalies regressed onto the interannual EADI. A zonally elongated band of significant positive temperature anomalies extends from East Asia across the North Pacific between approximately 30°N and 60°N, closely matching the spatial distribution of the dust plume. The

warming maximum exceeds 0.6 K over the central North Pacific near 45°N, 170°E, where dust loading is most concentrated. This spatial collocation ~~strongly~~ suggests that the mid-tropospheric warming is ~~largely~~ closely related to~~induced by~~ dust aerosol absorption. In response to this robust diabatic heating, the atmospheric column expands, thereby exciting an anomalous high-pressure system. This thermodynamic adjustment is clearly characterized by a large-scale anticyclonic circulation anomaly in the 500 hPa wind field over the North Pacific basin. Furthermore, the anomalous southerly winds near 165°E (Figure 5a), embedded within the western flank of this anticyclone, may advect warmer subtropical air poleward, providing a supplementary positive temperature tendency.


(a)
Averaged Temperature (850-400hPa)
K
70°N
60°N
50°N
40°N
30°N
20°N
120°E
150°E
180°
150°W
120°W
4
4
1 m s-1
(b)
Temperature 40-60°N
K
Pressure [hPa]
100
150
200
250
300
400
500
700
850
1000
0.1
0.3
1
120°E
150°E
180°
150°W
120°W
-0.6
-0.45
-0.3
-0.15
0
0.15
0.3
0.45
0.6

320

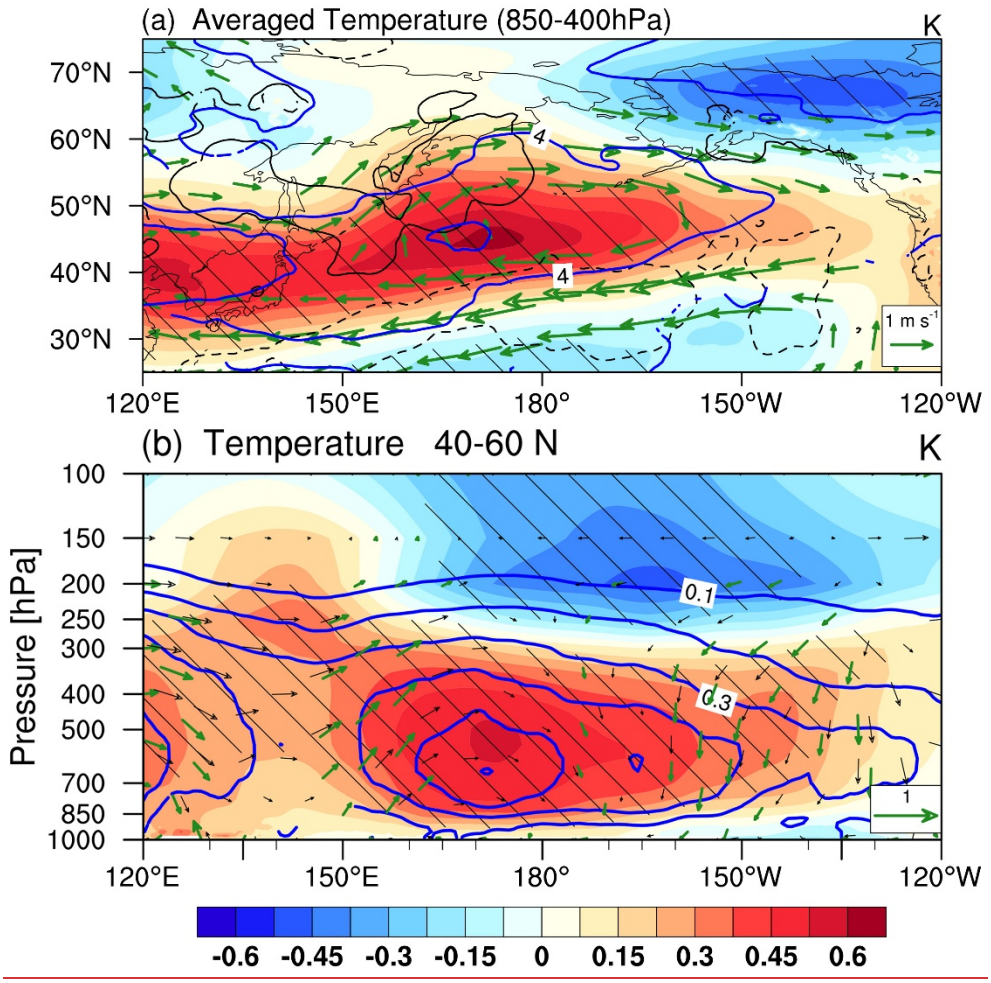
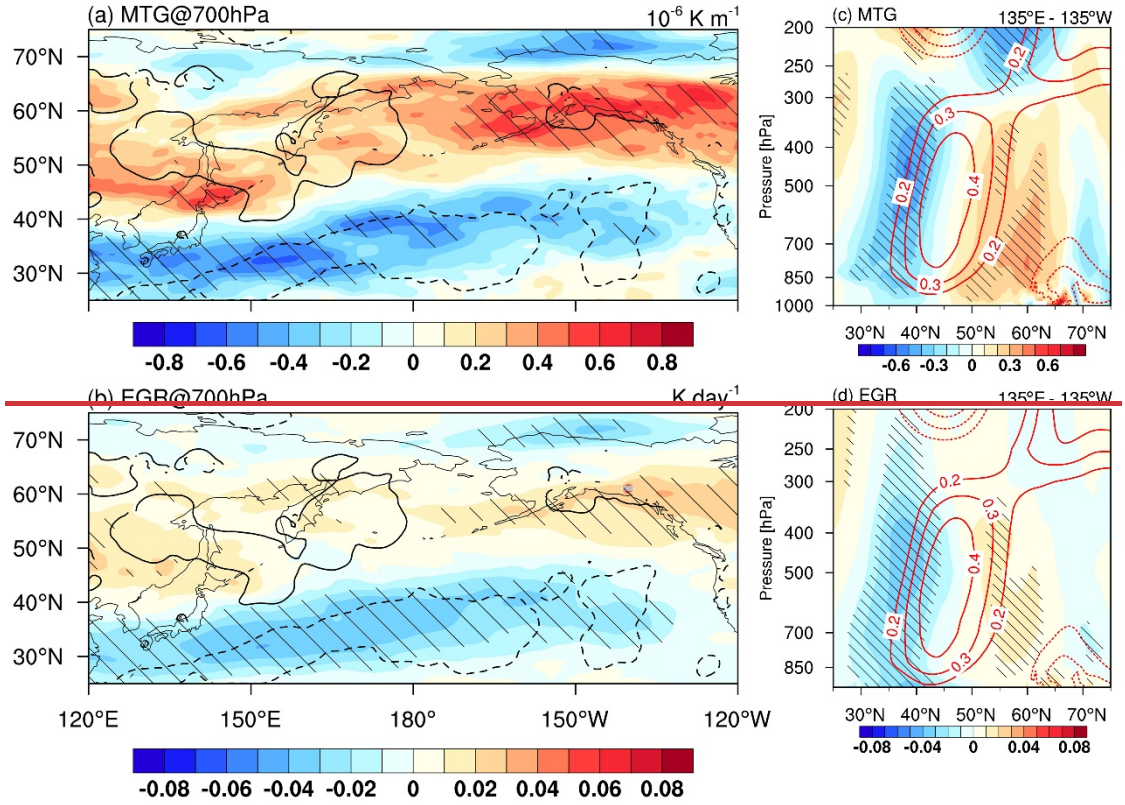


Figure 5. (a) Regressions of anomalies in averaged temperature between 850 and 400 hPa (shading; K), 500 hPa wind (vector; m s^{-1}), and dust column mass density (blue contours with an interval of 2 mg m^{-2}) onto the standardized EADI_IA. (b) Pressure-longitude cross section of the regressed anomalies in temperature (shading; K), zonal and vertical winds (vectors), and dust mass concentration (blue contours with an interval of 0.1 ug m^{-3}) averaged over the latitudinal band of 40° to 60°N. Black contours in (a) denote the statistically significant regions of the regressed $V'T'_{850}$ anomalies shown in Figure 3b. Hatching and green vectors indicate that the regressed anomalies in temperature and wind are statistically significant at the 95 % confidence level based on a Student's *t* test, respectively.

The vertical structure of the temperature response is further examined in Figure 5b, which shows the regression of meridionally averaged (40°–60°N) temperature and dust mass concentration anomalies onto the interannual EADI. The eastward-transported dust plume is primarily confined below 300 hPa level. This vertical distribution aligns well with previous satellite-based studies of individual trans-Pacific dust transport events (Guo et al., 2017; Voss and Evan, 2020). Correspondingly, the dust-related~~induced~~ atmospheric heating is highly concentrated in the middle and lower troposphere. A significant warm layer is collocated with the dust mass concentration anomalies, featuring a maximum warming center between 850 and 400 hPa. Beyond direct shortwave absorption, large-scale dynamical feedbacks may further reinforce this mid-tropospheric warming.

The anomalous anticyclonic circulation established over the central North Pacific (Figure 5a) is associated with subsidence to its east (east of ~180°E, Figure 5b), which likely contributes additional adiabatic warming through descending motion.

The dust-related~~dust-induced~~ mid-tropospheric warming is concentrated in a zonal band over the central North Pacific (Figure 5a), which is expected to modify the meridional temperature gradient (MTG)~~ and,~~. T~~t~~hrough thermal wind balance, the altered MTG adjusts the vertical wind shear and thereby the atmospheric baroclinicity. As shown in Figure 6a, the 700 hPa MTG ~~significantly~~ increases on the poleward flank and decreases on the equatorward flank of its climatological maximum (grey contours)~~along the northern flank of the North Pacific and decreases on the southern flank~~. This dipole pattern is a thermodynamically consistent consequence of the localized dust heating center identified above. The vertical cross-section averaged between 135°E and 135°W (Figure 6c) further confirms this structure, revealing a robust positive MTG anomaly north of 45°N and a negative anomaly to the south. These MTG anomalies are closely collocated with the northern and southern boundaries of the dust-related~~induced~~ warming center.



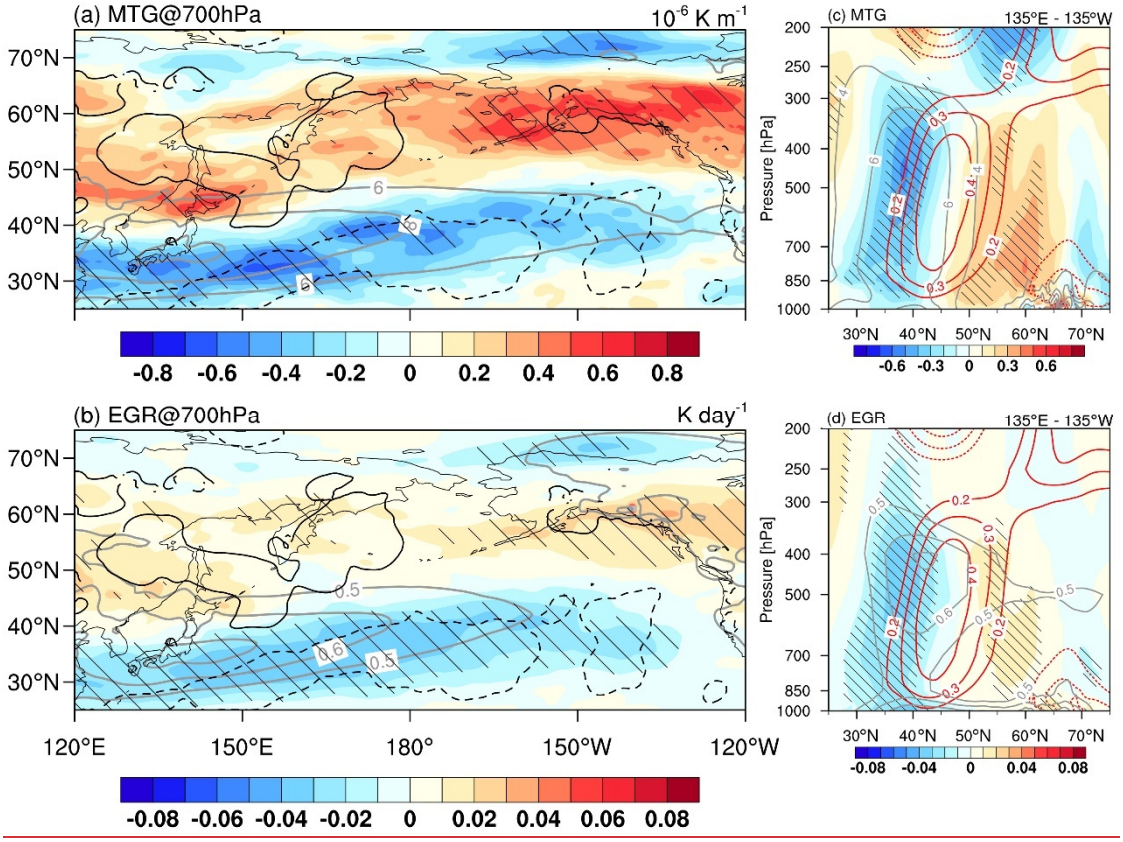


Figure 6. Regressions of anomalies in (a) the 700 hPa meridional temperature gradient (MTG; shading; 10^{-6} K m^{-1}) and (b) the 700 hPa maximum Eady growth rate (EGR; shading; K day^{-1}) onto the standardized EADI_IA. Panels (c) and (d) display the meridional vertical cross sections of the regressed (c) MTG and (d) EGR anomalies averaged from 135°E to 135°W. Black contours in (a) and (b) denote the statistically significant regions of the regressed $V'T'_{850}$ anomalies shown in Figure 3b. Red contours in (c) and (d) represent the regressed temperature anomalies (K), with solid and dashed lines indicating positive and negative values, respectively. Grey contours in (a, c) and (b, d) denote the climatological spring mean MTG (interval of 2 10^{-6} K m^{-1}) and EGR (interval of 0.1 K day^{-1}), respectively. Hatching indicates that the regressed MTG and EGR anomalies are statistically significant at the 95 % confidence level based on a Student's *t* test.

Because baroclinic instability is fundamentally governed by the MTG, the EGR exhibits an almost identical spatial response (Lindzen and Farrell, 1980; Simmonds and Lim, 2009). At 700 hPa (Figure 6b), the baroclinicity strengthens on the poleward flank and weakens on the equatorward flank of the climatological EGR maximum (grey contours), mirroring the dipole in the storm track metrics (Figure 3)~~in the north and weakens in the south~~. The vertical profile of the EGR anomalies (Figure 6d) closely mirrors that of the MTG throughout the lower and middle troposphere. Importantly, the spatial distribution of these EGR anomalies matches the regions of significant storm track changes, indicating that the baroclinic adjustment directly shapes the optimal zone for transient eddy growth (Chang et al., 2002)~~(Chang and Lee and Swanson, 2002)~~.

The preceding observational analysis outlines a consistent physical pathway for the dust effect on the North Pacific storm track. Springtime East Asian dust absorbs shortwave radiation, warming the mid-troposphere. This heating restructures the

meridional temperature gradient and alters atmospheric baroclinicity. As a result, the favorable zone for baroclinic eddy growth shifts to higher latitudes. We next examine whether this pathway can be reproduced by dust radiative forcing alone in WRF-Chem sensitivity experiments. ~~To futher to explicitly investigate and quantify this physical mechanism, we therefore employ targeted numerical simulations in the next section~~

3.3 Process-level verification of the proposed mechanism with WRF-Chem sensitivity experiments~~Quantitative analysis on the effect of dust radiative forcing~~

To test the pathway inferred above, we compare the CTRL and NoDust ensemble simulations for spring 2018. The CTRL experiment reasonably reproduces the observed spring circulation at 500 hPa, the trans-Pacific transport pathway of the dust plume, and the spatial patterns of both storm track metrics (Figure S7). The model is therefore suitable for examining the process-level response of the storm track to dust radiative forcing~~To isolate the causal role of the storm track response to dust radiative forcing, we conduct two sets of WRF-Chem ensemble simulations for the spring of 2018. Before examining the specific aerosol effects, we evaluate the baseline model performance. Figure 7 compares the spatial patterns of key variables between the observations (MERRA-2 and MODIS) and the CTRL simulation. The CTRL experiment reasonably reproduces the spring mid-tropospheric circulation, including the East Asian trough and the westerly stream at 500 hPa (Figures 7a and 7e). For AOD, the simulated magnitude is naturally lower than the MODIS total aerosol retrievals because the CTRL run includes only dust emissions. This simulated magnitude nevertheless remains quantitatively comparable to the observed dust AOD (Voss and Evan, 2020). The model also successfully captures the spatial distribution and the trans-Pacific transport pathway of the dust plume (Figures 7b and 7f). Furthermore, the spatial patterns of both the upper-tropospheric ($Z'Z'_{300}$) and lower-tropospheric ($V'T'_{850}$) storm track metrics are reasonably well captured (Figures 7c, 7d, 7g, and 7h). These results demonstrate that the WRF-Chem model is suitable for investigating the subsequent interactions between dust aerosols and the storm track~~.

The simulated responses are consistent with the pathway inferred from the reanalysis. Dust radiative forcing produces a pronounced warming in the mid-troposphere (850 to 400 hPa) over the North Pacific, accompanied by an anomalous anticyclonic circulation at 500 hPa (Figure 7c). The spatial pattern of this warming closely follows the simulated dust AOD. The heating modifies the atmospheric baroclinicity, so that the EGR at 700 hPa increases on the northern flank of the climatological storm track and decreases on the southern flank (Figure 7d). Correspondingly, both $Z'Z'_{300}$ and $V'T'_{850}$ shift poleward (Figures 7a and 7b). These results indicate that dust radiative heating alone can shift the North Pacific storm track

poleward, which supports the physical pathway inferred from the reanalysis.

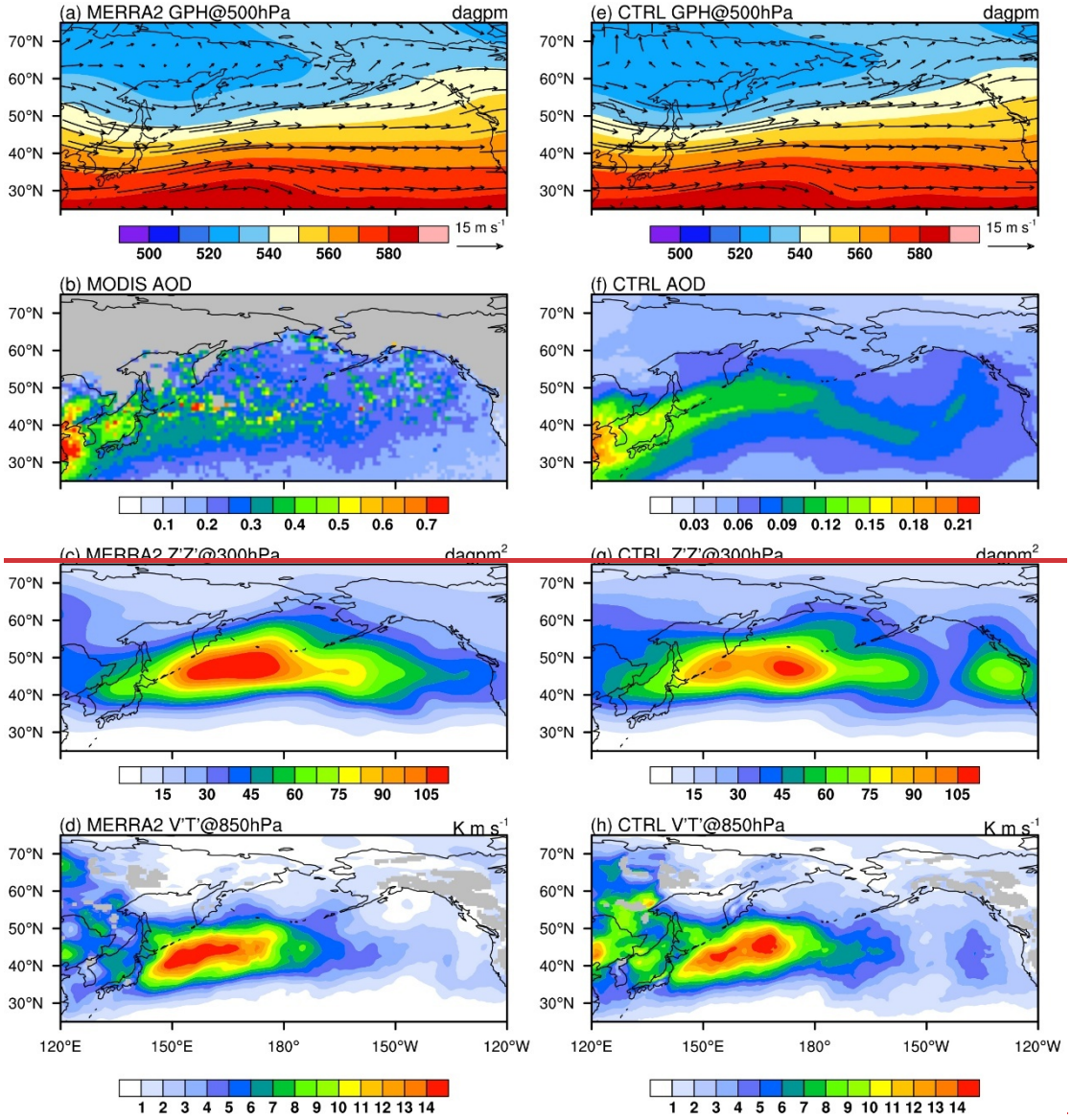


Figure 7. Spatial distributions of (a, e) 500 hPa geopotential height (shading; dagpm) and wind (vectors; m s^{-1}), (b, f) aerosol optical depth (AOD; shading; unitless), (c, g) $Z^{L}Z^{L}_{300}$ (shading; dagpm2), and (d, h) $V^{L}T^{L}_{850}$ (shading; K m s^{-1}) averaged over spring (MAM) of 2018. The left column (a, b, c, d) represents the observational and reanalysis data (MERRA-2 for meteorological fields and MODIS for AOD). The right column (e, f, g, h) shows the corresponding ensemble mean of the WRF-Chem CTRL experiment.

The model results corroborate the physical mechanism inferred from the observational analysis, reproducing both the spatial pattern and the sign of the storm track anomalies. As shown in Figure 8c, the dust radiative forcing induces a pronounced warming in the mid troposphere (850 to 400 hPa) over the North Pacific, accompanied by an anomalous anticyclonic

~~circulation at 500 hPa. The spatial pattern of this warming aligns well with the simulated dust AOD. This localized heating alters the environmental thermal field, thereby modifying the atmospheric baroclinicity. Consequently, the EGR at 700 hPa increases on the northern flank of the climatological storm track and decreases on the southern flank (Figure 8d). In response to these changes in baroclinic instability, both the upper-tropospheric ($Z'Z'_{300}$) and lower-tropospheric ($V'T'_{850}$) storm track metrics exhibit a clear poleward displacement (Figures 8a and 8b). Ultimately, the WRF-Chem sensitivity experiments provide causal evidence that dust-induced radiative heating shifts the North Pacific storm track poleward.~~

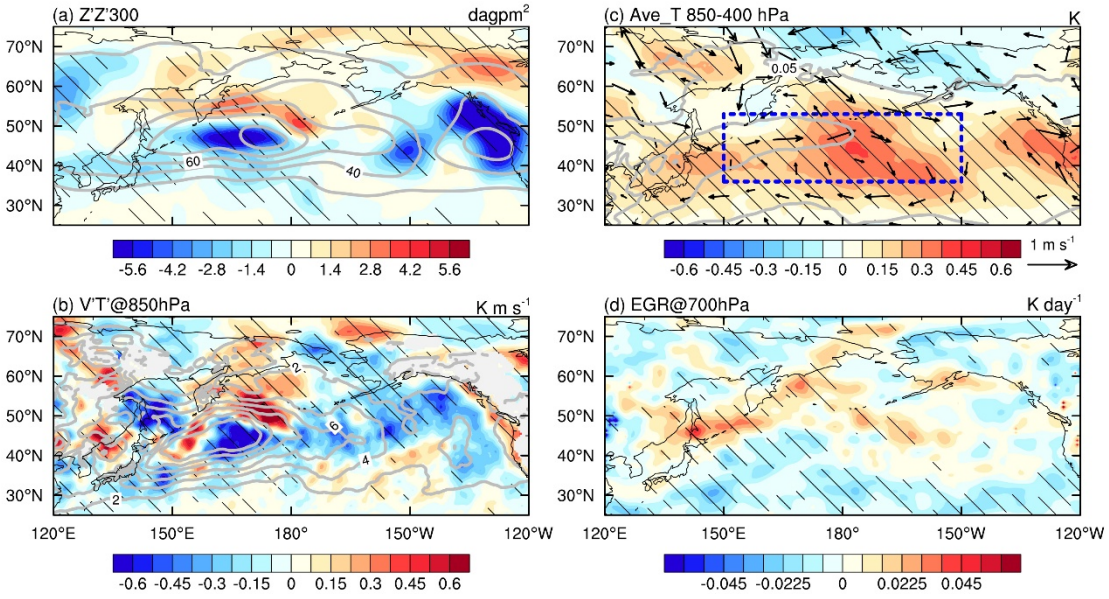
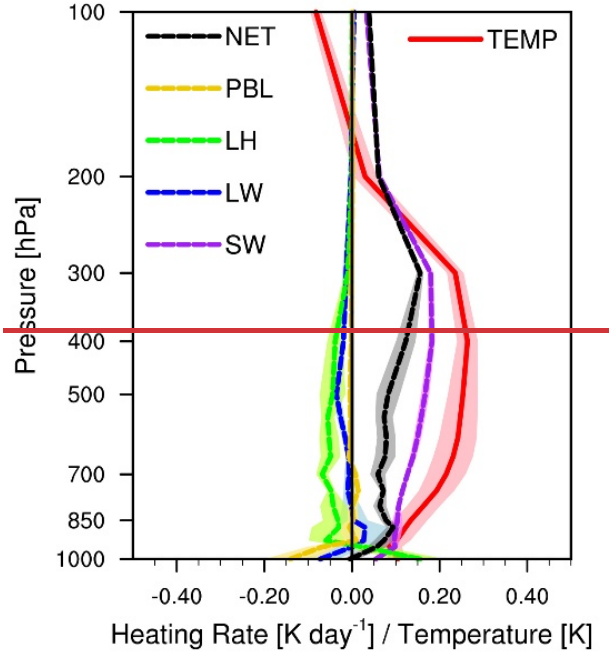


Figure ~~8~~7. Differences (CTRL minus NoDust) in (a) $Z'Z'_{300}$ (shading; dagpm^2), and (b) $V'T'_{850}$ (shading; K m s^{-1}), (c) averaged temperature between 850 and 400 hPa (shading; K), 500 hPa wind (vectors; m s^{-1}), and AOD (grey contours), and (d) 700 hPa EGR (shading; K day^{-1}). Grey contours in (a) and (b) represent the corresponding values in the CTRL experiment. The blue dashed box in (c) marks the region used for the heating rate budget in Figure S8. Hatching indicates that the differences are statistically significant at the 95 % confidence level based on a Student's *t* test.

The heating rate budget averaged over the main warming region (150°E–150°W, 35°–53°N; blue dashed box in Figure 7c) further identifies the source of this warming (Figure S8). Shortwave radiation is the only positive heating term and peaks near 400 hPa, whereas longwave radiation and latent heating make weak negative contributions. The net heating profile therefore closely follows the shortwave term, indicating that the simulated warming arises mainly from dust shortwave absorption.

~~To further examine the physical processes responsible for the mid-tropospheric warming shown in Figure 8c, Figure 9 presents the vertical profiles of temperature and atmospheric heating rate differences (CTRL minus NoDust) averaged over the main warming region in the North Pacific (150°E to 150°W, 35° to 53°N; blue dashed box in Figure 8c). The temperature profile shows a pronounced warming throughout the troposphere below 200 hPa, with a slight cooling above this level. This vertical structure is consistent with the observational regression results shown in Figure 5b. Among the contributing heating processes, shortwave radiation is the sole positive heating term, with its maximum at near 400 hPa. Longwave radiation and latent heating~~

~~both make modest negative contributions throughout the column. As a result, the net heating profile closely follows the shortwave radiative heating, confirming that the dust-induced atmospheric warming is primarily driven by shortwave absorption.~~



~~**Figure 9. Vertical profiles of differences (CTRL minus NoDust) in temperature (solid red line; K) and atmospheric heating rates (dashed line; K d^{-1}) averaged over the North Pacific (150°E–150°W, 35–53°N, as outlined in Figure 8c). Here, atmospheric heating rates include shortwave (SW) and longwave (LW) radiation heating, latent heating (LH, i.e., heating from the microphysics and cumulus scheme), and heating from the planetary boundary layer (PBL) scheme. Net heating rate (NET) = SW + LW + LH + PBL.**~~

4 Conclusions and discussion

This study shows ~~demonstrates~~ that interannual variations in springtime East Asian dust loading are systematically associated with a poleward shift of the North Pacific storm track~~springtime East Asian dust aerosols exert a systematic poleward influence on the North Pacific storm track on interannual timescales~~. Using MERRA-2 reanalysis data spanning 1980–2022, we identify a statistically robust association between anomalously high East Asian dust loading and a meridional dipole pattern in storm track activity, characterized by weakening on the equatorward flank and strengthening on the poleward flank. The underlying mechanism follows a coherent physical pathway (Figure ~~10~~8). Specifically, shortwave absorption by the trans-Pacific dust plume heats the mid-troposphere (850–400 hPa), which excites an anomalous anticyclonic circulation. This circulation restructures the meridional temperature gradient into a north-positive/south-negative dipole pattern, and consequently shifts the zone of maximum Eady growth rate poleward, favoring baroclinic eddy development at higher latitudes. Model sensitivity experiments for spring 2018 reproduce ~~both~~ the spatial pattern ~~and the sign~~ of this response, indicating ~~confirming~~ that dust shortwave absorption alone can produce a~~is sufficient to drive the observed~~ poleward ~~displacement~~ shift of the storm track.

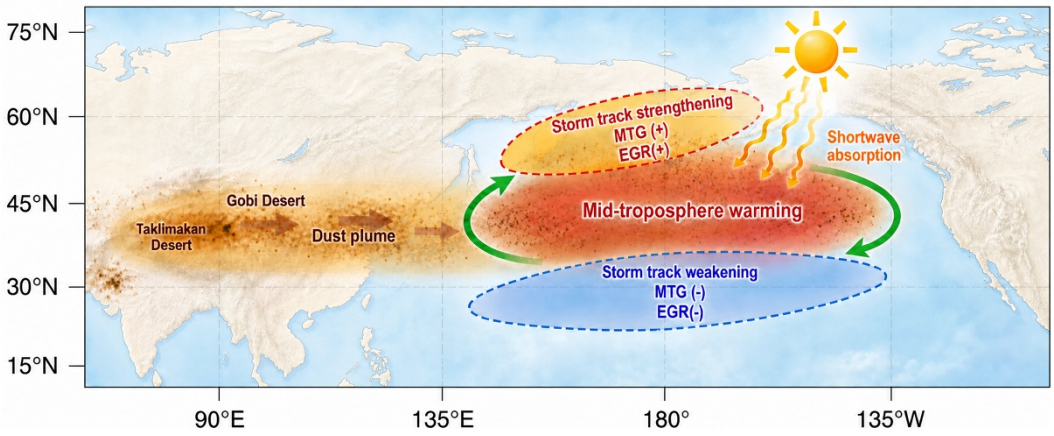


Figure ~~108~~.~~#~~Schematic diagram illustrating the physical mechanism by which springtime East Asian dust aerosols favour~~drive~~ a poleward shift of the North Pacific storm track. Dust emitted from East Asian sources is transported eastward across the North Pacific by mid-latitude westerlies. Shortwave absorption by the dust plume warms the mid-troposphere, enhancing (reducing) the meridional temperature gradient (MTG) on the poleward (equatorward) flank. The resulting dipole in the maximum Eady growth rate (EGR) favours storm track strengthening at higher latitudes and weakening at lower latitudes, producing a net poleward displacement.

It is important to distinguish the effects of dust aerosols from those of anthropogenic aerosols on the North Pacific storm track. Previous studies have shown that long-term changes in East Asian anthropogenic emissions predominantly intensify the wintertime storm track through aerosol-cloud interactions and associated latent heat release (Zhang et al., 2007; Wang et al., 2014b)~~(Zhang et al., 2007; Wang et al., 2014)~~. In contrast, our findings highlight that interannual variations in springtime dust aerosols mainly alter the latitudinal position of the storm track via aerosol-radiation interactions~~. This distinct~~, a response ~~is~~ attributable to~~driven by~~ the direct radiative heating of the dust layer. Because mid-latitude transient eddies transport heat, moisture, and momentum poleward~~Furthermore, mid-latitude transient eddies play a critical role in the poleward transport of heat, moisture, and momentum~~ (Shaw et al., 2016; Tamarin-Brodsky and Kaspi, 2017; Hoskins and Hodges, 2019), a shift in the storm track position redistributes these fluxes and carries consequences well beyond the North Pacific. T~~. The dust-induced poleward shift, particularly t~~he enhanced transient meridional heat flux near the Bering Sea (Figure 3b)~~,~~ may ~~substantially~~ accelerate springtime Arctic sea ice melting and trigger subsequent climate feedbacks (Overland and Pease, 1982; Huang et al., 2019; Peng et al., 2021). Downstream over North America, a poleward shift redirects the landfall of moisture transport and has been linked to drier conditions over the southwestern United States and wetter conditions along the higher latitude coast (Salathé Jr., 2006; Chemke and Yuval, 2026). The storm track position also regulates the frequency of deep tropopause folds that bring stratospheric ozone into the lower troposphere over western North America, an effect that peaks in spring (Lin et al., 2015; Breeden et al., 2021)~~(Lin et al., 2015; Breeden et al., 2021)~~. Assessing these consequences requires dedicated analysis beyond the scope of the present study, but they indicate that springtime dust variability, including its interannual component, deserves attention in regional climate assessments.~~These potential impacts warrant further investigation.~~

~~It is worth noting that t~~The WRF-Chem experiments are intended to verify the proposed mechanism rather than to quantify the sensitivity of the storm track to dust. The simulated responses in both temperature and storm track metrics are weaker than those inferred from the observational regression analysis, even after the difference in North Pacific dust burden between the 2018 experiment and a one-standard-deviation EADI anomaly is considered. Several factors may contribute to this discrepancy. The regional model domain excludes dust transported~~First, the dust loading over East Asia and the North Pacific originates not only from local East Asian sources but also from long-range transport~~ from the Middle East and North Africa (Creamean et al., 2013; Hu et al., 2019; Zhou et al., 2024; Huang et al., 2025), which lowers the simulated dust burden over the North Pacific. ~~Our regional model domain does not fully capture these remote contributions, which would lead to an underestimation of the total dust burden and the associated radiative heating over the North Pacific. Second, the shortwave absorptive capacity of dust is likely underestimated in our simulations. Observational studies have shown that~~ East Asian dust ~~readily~~ also mixes with anthropogenic aerosol ~~specie~~s during long-range transport, and such internally mixed dust aerosols can be more than 50% more absorbing than pure dust (Tian et al., 2018). This enhancement is not represented because anthropogenic emissions were excluded by design~~Since our WRF-Chem experiments excluded anthropogenic emissions by design, this absorption enhancement associated with mixing was not represented~~. In addition, ~~Third,~~ the four-band shortwave radiation scheme used in our WRF-Chem configuration tends to underestimate dust shortwave heating rates relative to schemes with finer spectral resolution (Feng et al., 2025)~~, which would further weaken the simulated thermal response~~. ~~Nevertheless, the primary purpose of the WRF-Chem experiments in this study is to provide a process-level verification of the physical mechanism identified from the observational analysis, rather than to achieve precise quantitative agreement.~~

Finally,~~Beyond direct radiative heating,~~ dust particles can ~~also~~ act as ice nucleating particles and alter the ~~atmospheric~~ energy budget through aerosol-cloud interactions (Uno et al., 2009; Zeng et al., 2023; Chen et al., 2024), which are not included in the current configuration.

The magnitude of the simulated response also differs considerably between models. A pair of CESM2 experiments with and without dust emission reproduces the same meridional dipole in both storm track metrics (Figure S9), but the response is about four to five times larger than in WRF-Chem for a similar North Pacific dust burden. Part of this spread likely arises from dust optical properties. Climate models using conventional refractive indices such as Optical Properties of Aerosols and Clouds (OPAC) tend to overestimate the absorption of Asian dust (Yuan et al., 2026), whereas the refractive index adopted in our WRF-Chem configuration (Zhao et al., 2012) is less absorptive (Jin et al., 2016). The two models may therefore bracket the true dust heating from opposite sides. After rescaling to a common dust burden, the amplitudes follow the order regression, CESM2 and WRF-Chem. The regression estimate should be regarded as an upper bound, because it may include circulation anomalies that covary with dust, and the response need not scale linearly between a single high-dust spring and a one-standard-deviation anomaly. Taken together, the reanalysis and the two models consistently support the radiative pathway, but the quantitative sensitivity of the storm track position to interannual dust variability remains uncertain by a factor of several.

Constraining it will require multi-model, multi-year dust sensitivity experiments with observation-constrained dust optical properties, realistic aerosol mixing, and aerosol-cloud interactions.

~~Our current model configuration did not account for these indirect microphysical effects. Therefore, achieving a more precise quantitative assessment of the storm track response will require future studies to incorporate refined dust optical properties, realistic aerosol mixing representations, and these complex aerosol-cloud interactions.~~

Code and data availability

The source codes of WRF-Chem model are available at https://www2.mmm.ucar.edu/wrf/users/download/get_source.html (UCAR, 2026). The source codes of CESM2 model are available at https://doi.org/10.5281/zenodo.3895315 (Danabasoglu et al., 2019). The FNL data are available at https://rda.ucar.edu/datasets/ds083.2/ (NCEP, 2000)~~(Ncep, 2000)~~. MERRA-2 reanalysis data are available at https://disc.gsfc.nasa.gov/datasets (GMAO, 2015). The MODIS AOD are available at https://ladsweb.modaps.eosdis.nasa.gov/missions-and-measurements/products/MOD08_M3 (Platnick~~,~~ et al., 2015). CMAP precipitation data are available at https://disc.gsfc.nasa.gov/datasets (Xie and Arkin, 1997). The NAO index and ONI are available at https://www.cpc.ncep.noaa.gov/products/precip/CWlink/pna/nao.shtml and https://www.cpc.ncep.noaa.gov/products/analysis_monitoring/ensostuff/ONI_v5.php, respectively (NOAA CPC, 2026a, b). Dust emission data are available at https://doi.org/10.11888/Terre.tpdc.301534 (Fu, 2026).

Author contributions

XH, HX and AZ conceptualized the research goals and developed the methodology, including the experimental setup. AZ carried out the investigation, performed the formal analysis, and visualized the results. JD and AD also contributed to the supervision of the work. LX, ZW, KD and TL contributed to data curation. AZ prepared the manuscript with contributions from all co-authors, and all authors contributed to the writing (review and editing) of the final article.

Competing interests

The contact author has declared that none of the authors has any competing interests.

Acknowledgements

We are grateful to the High Performance Computing Center (HPCC) of Nanjing University for doing the numerical calculations in this paper on its blade cluster system. We also thank all the corresponding institutions for providing their data for this study. Additionally, we acknowledge the use of the GPT image 2 model (OpenAI) for the visual optimization of the schematic

diagram presented in Figure ~~10~~8, while emphasizing that the scientific concepts and physical mechanisms depicted therein remain entirely the work of the authors.

Financial support

This work was supported by the National Natural Science Foundation of China (42588101) and the New Cornerstone Science Foundation through the XPLORER PRIZE.

Review statement

References

Awan, J. A. and Bae, D.-H.: Features and interdecadal variability of droughts in the homogeneous rainfall zones over the East Asian monsoon region, Int. J. Climatol., 36, 1943–1953, https://doi.org/10.1002/joc.4471, 2016.

Bao, Z., Wen, Z., and Wu, R.: Variability of aerosol optical depth over east Asia and its possible impacts, J. Geophys. Res.-Atmos., 114, D14214, https://doi.org/10.1029/2008JD010603, 2009.

Bender, F. A.-M., Ramanathan, V., and Tselioudis, G.: Changes in extratropical storm track cloudiness 1983–2008: observational support for a poleward shift, Clim. Dynam., 38, 2037–2053, https://doi.org/10.1007/s00382-011-1065-6, 2012.

Blackmon, M. L.: A Climatological Spectral Study of the 500 mb Geopotential Height of the Northern Hemisphere, J. Atmos. Sci., 33, 1607–1623, https://doi.org/10.1175/1520-0469(1976)033<1607:ACSSOT>2.0.CO;2, 1976.

Bohren, C. F. and Huffman, D. R.: Absorption and Scattering of Light by Small Particles, John Wiley & Sons, New York, USA, 1983.

Breeden, M. L., Butler, A. H., Albers, J. R., Sprenger, M., and Langford, A. O.: The spring transition of the North Pacific jet and its relation to deep stratosphere-to-troposphere mass transport over western North America, Atmos. Chem. Phys., 21, 2781-2794, https://doi.org/10.5194/acp-21-2781-2021, 2021.

Cai, W., van Rensch, P., Cowan, T., and Hendon, H. H.: Teleconnection Pathways of ENSO and the IOD and the Mechanisms for Impacts on Australian Rainfall, J. Climate, 24, 3910–3923, https://doi.org/10.1175/2011JCLI4129.1, 2011.

Chang, E. K. M., Lee, S., and Swanson, K. L.: Storm Track Dynamics, J. Climate, 15, 2163–2183, https://doi.org/10.1175/1520-0442(2002)015<2163:STD>2.0.CO;2, 2002.

Chemke, R. and Yuval, J.: Climate change shifts the North Pacific storm track polewards, Nature, 649, 626–630, https://doi.org/10.1038/s41586-025-09895-y, 2026.

Chen, J., Xu, J., Wu, Z., Meng, X., Yu, Y., Ginoux, P., DeMott, P. J., Xu, R., Zhai, L., Yan, Y., Zhao, C., Li, S.-M., Zhu, T., and Hu, M.: Decreased dust particles amplify the cloud cooling effect by regulating cloud ice formation over the Tibetan Plateau, Sci. Adv., 10, eado0885, https://doi.org/10.1126/sciadv.ado0885, 2024.

Chen, S., Huang, J., Qian, Y., Zhao, C., Kang, L., Yang, B., Wang, Y., Liu, Y., Yuan, T., Wang, T., Ma, X., and Zhang, G.: An overview of mineral dust modeling over East Asia, J. Meteorol. Res., 31, 633–653, https://doi.org/10.1007/s13351-017-6142-2, 2017.

Chen, S.-H. and Sun, W.-Y.: A One-dimensional Time Dependent Cloud Model, Journal of the Meteorological Society of Japan. Ser. II, 80, 99-118, https://doi.org/10.2151/jmsj.80.99, 2002.

Chen, Y., Yang, K., Zhou, D., Qin, J., and Guo, X.: Improving the Noah Land Surface Model in Arid Regions with an Appropriate Parameterization of the Thermal Roughness Length, J. Hydrometeorol., 11, 995–1006, https://doi.org/10.1175/2010JHM1185.1, 2010.

Chen, Y., Chen, S., Zhou, J., Zhao, D., Bi, H., Zhang, Y., Alam, K., Yu, H., Yang, Y., and Chen, J.: A super dust storm enhanced by radiative feedback, npj Clim. Atmos. Sci., 6, 90, https://doi.org/10.1038/s41612-023-00418-y, 2023.

Chin, M., Ginoux, P., Kinne, S., Torres, O., Holben, B. N., Duncan, B. N., Martin, R. V., Logan, J. A., Higurashi, A., and Nakajima, T.: Tropospheric Aerosol Optical Thickness from the GOCART Model and Comparisons with Satellite and Sun Photometer Measurements, J. Atmos. Sci., 59, 461–483, https://doi.org/10.1175/1520-0469(2002)059<0461:TAOTFT>2.0.CO;2, 2002.

Creamean, J. M., Suski, K. J., Rosenfeld, D., Cazorla, A., DeMott, P. J., Sullivan, R. C., White, A. B., Ralph, F. M., Minnis, P., Comstock, J. M., Tomlinson, J. M., and Prather, K. A.: Dust and Biological Aerosols from the Sahara and Asia Influence Precipitation in the Western U.S., Science, 339, 1572–1578, https://doi.org/10.1126/science.1227279, 2013.

Danabasoglu, G., Lamarque, J.-F., Bacmeister, J., Bailey, D. A., DuVivier, A. K., Edwards, J., Emmons, L. K., Fasullo, J., Garcia, R., Gettelman, A., Hannay, C., Holland, M. M., Large, W. G., Lauritzen, P. H., Lawrence, D. M., Lenaerts, J. T. M., Lindsay, K., Lipscomb, W. H., Mills, M. J., Neale, R., Oleson, K. W., Otto-Bliesner, B., Phillips, A. S., Sacks, W., Tilmes, S., van Kampenhout, L., Vertenstein, M., Bertini, A., Dennis, J., Deser, C., Fischer, C., Fox-Kemper, B., Kay, J. E., Kinnison, D., Kushner, P. J., Larson, V. E., Long, M. C., Mickelson, S., Moore, J. K., Nienhouse, E., Polvani, L., Rasch, P. J., and Strand, W. G.: CESM-release-cesm2.1.1, Zenodo [code], https://doi.org/10.5281/zenodo.3895315, 2019.

Danabasoglu, G., Lamarque, J.-F., Bacmeister, J., Bailey, D. A., DuVivier, A. K., Edwards, J., Emmons, L. K., Fasullo, J., Garcia, R., Gettelman, A., Hannay, C., Holland, M. M., Large, W. G., Lauritzen, P. H., Lawrence, D. M., Lenaerts, J. T. M., Lindsay, K., Lipscomb, W. H., Mills, M. J., Neale, R., Oleson, K. W., Otto-Bliesner, B., Phillips, A. S., Sacks, W., Tilmes, S., van Kampenhout, L., Vertenstein, M., Bertini, A., Dennis, J., Deser, C., Fischer, C., Fox-Kemper, B., Kay, J. E., Kinnison, D., Kushner, P. J., Larson, V. E., Long, M. C., Mickelson, S., Moore, J. K., Nienhouse, E., Polvani, L., Rasch, P. J., and Strand, W. G.: The Community Earth System Model Version 2 (CESM2), Journal of Advances in Modeling Earth Systems, 12, e2019MS001916, https://doi.org/10.1029/2019MS001916, 2020.

Feng, J., Zhao, C., Du, Q., Yang, Z., and Jin, C.: Amending the algorithm of aerosol–radiation interactions in WRF-Chem (v4.4), Geosci. Model Dev., 18, 585–603, https://doi.org/10.5194/gmd-18-585-2025, 2025.

Fu, Y.: Processed dust emission data and code for "Beyond the horizon: long-term benefits of vegetation restoration for dust mitigation in Eastern Asia", National Tibetan Plateau Data Center [dataset], 10.11888/Terre.tpdc.301534, 2026.

Fu, Y., Wu, C., Gao, S., Peñuelas, J., Camarero, J. J., Zhang, J., Li, D., Zheng, X., Li, Z., Wang, Y., Liang, E., and Piao, S.: Vegetation greening drives long-term dust mitigation in Eastern Asia, Nat. Commun., 17, 1729, https://doi.org/10.1038/s41467-026-68427-y, 2026.

Gelaro, R., McCarty, W., Suárez, M. J., Todling, R., Molod, A., Takacs, L., Randles, C. A., Darmenov, A., Bosilovich, M. G., Reichle, R., Wargan, K., Coy, L., Cullather, R., Draper, C., Akella, S., Buchard, V., Conaty, A., da Silva, A. M., Gu, W., Kim, G.-K., Koster, R., Lucchesi, R., Merkova, D., Nielsen, J. E., Partyka, G., Pawson, S., Putman, W., Rienecker, M., Schubert, S. D., Sienkiewicz, M., and Zhao, B.: The Modern-Era Retrospective Analysis for Research and Applications, Version 2 (MERRA-2), J. Climate, 30, 5419–5454, https://doi.org/10.1175/JCLI-D-16-0758.1, 2017.

Global Modeling and Assimilation Office (GMAO): MERRA-2 instM_3d_asm_Np: 3d, Monthly mean, Instantaneous, Pressure-Level, Assimilation, Assimilated Meteorological Fields V5.12.4, Goddard Earth Sciences Data and Information Services Center (GES DISC) [data set], https://doi.org/10.5067/2E096JV59PK7, 2015.

Grell, G. A.: Prognostic Evaluation of Assumptions Used by Cumulus Parameterizations, Mon. Weather Rev., 121, 764–787, https://doi.org/10.1175/1520-0493(1993)121<0764:PEOAUB>2.0.CO;2, 1993.

Grell, G. A. and Dévényi, D.: A generalized approach to parameterizing convection combining ensemble and data assimilation techniques, Geophys. Res. Lett., 29, 38-1–38-4, https://doi.org/10.1029/2002GL015311, 2002.

Gui, K., Yao, W., Che, H., An, L., Zheng, Y., Li, L., Zhao, H., Zhang, L., Zhong, J., Wang, Y., and Zhang, X.: Record-breaking dust loading during two mega dust storm events over northern China in March 2021: aerosol optical and radiative properties and meteorological drivers, Atmos. Chem. Phys., 22, 7905–7932, https://doi.org/10.5194/acp-22-7905-2022, 2022.

Guo, J., Xu, H., Liu, L., Chen, D., Peng, Y., Yim, S. H.-L., Yang, Y., Li, J., Zhao, C., and Zhai, P.: The Trend Reversal of Dust Aerosol Over East Asia and the North Pacific Ocean Attributed to Large-Scale Meteorology, Deposition, and Soil Moisture, J. Geophys. Res.-Atmos., 124, 10450–10466, https://doi.org/10.1029/2019JD030654, 2019.

Guo, J., Lou, M., Miao, Y., Wang, Y., Zeng, Z., Liu, H., He, J., Xu, H., Wang, F., Min, M., and Zhai, P.: Trans-Pacific transport of dust aerosols from East Asia: Insights gained from multiple observations and modeling, Environ. Pollut., 230, 1030–1039, https://doi.org/10.1016/j.envpol.2017.07.062, 2017.

Gupta, P., Levy, R. C., Mattoo, S., Remer, L. A., and Munchak, L. A.: A surface reflectance scheme for retrieving aerosol optical depth over urban surfaces in MODIS Dark Target retrieval algorithm, Atmos. Meas. Tech., 9, 3293–3308, https://doi.org/10.5194/amt-9-3293-2016, 2016.

Heidinger, A. K., Foster, M. J., Walther, A., and Zhao, X.: The Pathfinder Atmospheres–Extended AVHRR Climate Dataset, B. Am. Meteorol. Soc., 95, 909–922, https://doi.org/10.1175/BAMS-D-12-00246.1, 2014.

Holben, B. N., Eck, T. F., Slutsker, I., Tanré, D., Buis, J. P., Setzer, A., Vermote, E., Reagan, J. A., Kaufman, Y. J., Nakajima, T., Lavenu, F., Jankowiak, I., and Smirnov, A.: AERONET—A Federated Instrument Network and Data Archive for Aerosol Characterization, Remote Sens. Environ., 66, 1–16, https://doi.org/10.1016/S0034-4257(98)00031-5, 1998.

Hong, S.-Y., Noh, Y., and Dudhia, J.: A New Vertical Diffusion Package with an Explicit Treatment of Entrainment Processes, Mon. Weather Rev., 134, 2318–2341, https://doi.org/10.1175/MWR3199.1, 2006.

Hoskins, B. J. and Hodges, K. I.: The Annual Cycle of Northern Hemisphere Storm Tracks. Part I: Seasons, J. Climate, 32, 1743–1760, https://doi.org/10.1175/JCLI-D-17-0870.1, 2019.

Hu, Z., Huang, J., Zhao, C., Ma, Y., Jin, Q., Qian, Y., Leung, L. R., Bi, J., and Ma, J.: Trans-Pacific transport and evolution of aerosols: spatiotemporal characteristics and source contributions, Atmos. Chem. Phys., 19, 12709–12730, https://doi.org/10.5194/acp-19-12709-2019, 2019.

Huang, J., Wang, T., Wang, W., Li, Z., and Yan, H.: Climate effects of dust aerosols over East Asian arid and semiarid regions, J. Geophys. Res.-Atmos., 119, 11398–11416, https://doi.org/10.1002/2014JD021796, 2014.

Huang, Y., Dong, X., Xi, B., and Deng, Y.: A survey of the atmospheric physical processes key to the onset of Arctic sea ice melt in spring, Clim. Dynam., 52, 4907–4922, https://doi.org/10.1007/s00382-018-4422-x, 2019.

Huang, Z., Liu, Q., Dong, Q., Hu, Z., Zhang, X., Li, Z., and Wang, Y.: Eastward Transport of African Dust and Its Climatic and Environmental Impacts, Adv. Earth Sci. (in Chinese), 40, 1–14, https://doi.org/10.11867/j.issn.1001-8166.2025.004, 2025.

Iacono, M. J., Delamere, J. S., Mlawer, E. J., Shephard, M. W., Clough, S. A., and Collins, W. D.: Radiative forcing by long-lived greenhouse gases: Calculations with the AER radiative transfer models, J. Geophys. Res.-Atmos., 113, D13103, https://doi.org/10.1029/2008JD009944, 2008.

Idrissa, N. F., Zhao, C., Zhiyuan, H., Feng, J., and Du, Q.: Long-range transport impact of a severe dust storm over the Yangtze River Basin region and its modeling sensitivity to dust emission scheme, Atmos. Res., 310, 107612, https://doi.org/10.1016/j.atmosres.2024.107612, 2024.

Jiang, T., Deng, Y., and Li, W.: Local kinetic energy budget of high-frequency and intermediate-frequency eddies: winter climatology and interannual variability, Clim. Dynam., 41, 961–976, https://doi.org/10.1007/s00382-013-1684-1, 2013.

Jin, Q., Yang, Z.-L., and Wei, J.: High sensitivity of Indian summer monsoon to Middle East dust absorptive properties, Scientific Reports, 6, 30690, https://doi.org/10.1038/srep30690, 2016.

Jin, Q., Wei, J., Lau, W. K. M., Pu, B., and Wang, C.: Interactions of Asian mineral dust with Indian summer monsoon: Recent advances and challenges, Earth-Sci. Rev., 215, 103562, https://doi.org/10.1016/j.earscirev.2021.103562, 2021.

Kahn, R. A., Gaitley, B. J., Martonchik, J. V., Diner, D. J., Crean, K. A., and Holben, B.: Multiangle Imaging Spectroradiometer (MISR) global aerosol optical depth validation based on 2 years of coincident Aerosol Robotic Network (AERONET) observations, J. Geophys. Res.-Atmos., 110, D10S04, https://doi.org/10.1029/2004JD004706, 2005.

Kok, J. F., Storelvmo, T., Karydis, V. A., Adebiyi, A. A., Mahowald, N. M., Evan, A. T., He, C., and Leung, D. M.: Mineral dust aerosol impacts on global climate and climate change, Nat. Rev. Earth Environ., 4, 71–86, https://doi.org/10.1038/s43017-022-00379-5, 2023.

Lau, K. M., Kim, M. K., and Kim, K. M.: Asian summer monsoon anomalies induced by aerosol direct forcing: the role of the Tibetan Plateau, Clim. Dynam., 26, 855–864, https://doi.org/10.1007/s00382-006-0114-z, 2006.

Levy, R. C., Remer, L. A., Kleidman, R. G., Mattoo, S., Ichoku, C., Kahn, R., and Eck, T. F.: Global evaluation of the Collection 5 MODIS dark-target aerosol products over land, Atmos. Chem. Phys., 10, 10399–10420, https://doi.org/10.5194/acp-10-10399-2010, 2010.

Li, Y., Xu, F., Feng, J., Du, M., Song, W., Li, C., and Zhao, W.: Influence of the previous North Atlantic Oscillation (NAO) on the spring dust aerosols over North China, Atmos. Chem. Phys., 23, 6021–6042, https://doi.org/10.5194/acp-23-6021-2023, 2023.

Liguori, G., McGregor, S., Singh, M., Arblaster, J., and Di Lorenzo, E.: Revisiting ENSO and IOD Contributions to Australian Precipitation, Geophys. Res. Lett., 49, e2021GL094295, https://doi.org/10.1029/2021GL094295, 2022.

~~Lin, Y. and Colle, B. A.: A New Bulk Microphysical Scheme That Includes Riming Intensity and Temperature-Dependent Ice Characteristics, Mon. Weather Rev., 139, 1013–1035, https://doi.org/10.1175/2010MWR3293.1, 2011.~~Lin, M., Fiore, A. M., Horowitz, L. W., Langford, A. O., Oltmans, S. J., Tarasick, D., and Rieder, H. E.: Climate variability modulates western US ozone air quality in spring via deep stratospheric intrusions, Nature Communications, 6, 7105, https://doi.org/10.1038/ncomms8105, 2015.

Lindzen, R. S. and Farrell, B.: A Simple Approximate Result for the Maximum Growth Rate of Baroclinic Instabilities, J. Atmos. Sci., 37, 1648–1654, https://doi.org/10.1175/1520-0469(1980)037<1648:ASARFT>2.0.CO;2, 1980.

Liu, Z., Ming, Y., Wang, L., Bollasina, M., Luo, M., Lau, N.-C., and Yim, S. H.-L.: A Model Investigation of Aerosol-Induced Changes in the East Asian Winter Monsoon, Geophys. Res. Lett., 46, 10186–10195, https://doi.org/10.1029/2019GL084228, 2019.

Ming, Y., Ramaswamy, V., and Chen, G.: A Model Investigation of Aerosol-Induced Changes in Boreal Winter Extratropical Circulation, J. Climate, 24, 6077–6091, https://doi.org/10.1175/2011JCLI4111.1, 2011.

NCEP/National Weather Service/NOAA/U.S. Department of Commerce: NCEP FNL Operational Model Global Tropospheric Analyses, continuing from July 1999, NSF National Center for Atmospheric Research [data set], https://doi.org/10.5065/D6M043C6, 2000.

NOAA CPC: North Atlantic Oscillation (NAO) monthly index, NOAA Climate Prediction Center [data set], https://www.cpc.ncep.noaa.gov/products/precip/CWlink/pna/nao.shtml, last access: 25 September 2026a.

NOAA CPC: Oceanic Niño Index (ONI), version 5, NOAA Climate Prediction Center [data set], https://www.cpc.ncep.noaa.gov/products/analysis_monitoring/ensostuff/ONI_v5.php, last access: 25 September 2026b.

Overland, J. E. and Pease, C. H.: Cyclone Climatology of the Bering Sea and Its Relation to Sea Ice Extent, Mon. Weather Rev., 110, 5–13, https://doi.org/10.1175/1520-0493(1982)110<0005:CCOTBS>2.0.CO;2, 1982.

Pahlow, M., Parlange, M. B., and Porté-Agel, F.: On Monin–Obukhov Similarity In The Stable Atmospheric Boundary Layer, Bound.-Lay. Meteorol., 99, 225–248, https://doi.org/10.1023/A:1018909000098, 2001.

Peng, L., Zhang, X., Kim, J.-H., Cho, K.-H., Kim, B.-M., Wang, Z., and Tang, H.: Role of Intense Arctic Storm in Accelerating Summer Sea Ice Melt: An In Situ Observational Study, Geophys. Res. Lett., 48, e2021GL092714, https://doi.org/10.1029/2021GL092714, 2021.

Pfahl, S., Madonna, E., Boettcher, M., Joos, H., and Wernli, H.: Warm Conveyor Belts in the ERA-Interim Dataset (1979–2010). Part II: Moisture Origin and Relevance for Precipitation, J. Climate, 27, 27–40, https://doi.org/10.1175/JCLI-D-13-00223.1, 2014.

Platnick, S., Meyer, K. G., King, M. D., Wind, G., Amarasinghe, N., Marchant, B., Arnold, G. T., Zhang, Z., Hubanks, P. A., Holz, R. E., Yang, P., Ridgway, W. L., and Riedi, J.: MODIS Atmosphere L3 Monthly Product (MOD08_M3), NASA MODIS Adaptive Processing System, Goddard Space Flight Center [data set], https://doi.org/10.5067/MODIS/MOD08_M3.061, 2015.

Salathé Jr., E. P.: Influences of a shift in North Pacific storm tracks on western North American precipitation under global warming, Geophys. Res. Lett., 33, L19820, https://doi.org/10.1029/2006GL026882, 2006.

Seager, R., Naik, N., Ting, M., Cane, M. A., Harnik, N., and Kushnir, Y.: Adjustment of the atmospheric circulation to tropical Pacific SST anomalies: Variability of transient eddy propagation in the Pacific–North America sector, Q. J. Roy. Meteor. Soc., 136, 277–296, https://doi.org/10.1002/qj.588, 2010.

Shao, Y.: Simplification of a dust emission scheme and comparison with data, J. Geophys. Res.-Atmos., 109, D10202, https://doi.org/10.1029/2003JD004372, 2004.

Shaw, T. A., Baldwin, M., Barnes, E. A., Caballero, R., Garfinkel, C. I., Hwang, Y. T., Li, C., O'Gorman, P. A., Rivière, G., Simpson, I. R., and Voigt, A.: Storm track processes and the opposing influences of climate change, Nat. Geosci., 9, 656–664, https://doi.org/10.1038/ngeo2783, 2016.

Simmonds, I. and Lim, E.-P.: Biases in the calculation of Southern Hemisphere mean baroclinic eddy growth rate, Geophys. Res. Lett., 36, L01707, https://doi.org/10.1029/2008GL036320, 2009.

Simmons, A. J. and Hoskins, B. J.: The Life Cycles of Some Nonlinear Baroclinic Waves, J. Atmos. Sci., 35, 414–432, https://doi.org/10.1175/1520-0469(1978)035<0414:TLCOSN>2.0.CO;2, 1978.

Sokolik, I. N. and Toon, O. B.: Incorporation of mineralogical composition into models of the radiative properties of mineral aerosol from UV to IR wavelengths, J. Geophys. Res.-Atmos., 104, 9423–9444, https://doi.org/10.1029/1998JD200048, 1999.

Stockwell, W. R., Middleton, P., Chang, J. S., and Tang, X.: The second generation regional acid deposition model chemical mechanism for regional air quality modeling, J. Geophys. Res.-Atmos., 95, 16343–16367, https://doi.org/10.1029/JD095iD10p16343, 1990.

Sun, Y. and Zhao, C.: Influence of Saharan Dust on the Large-Scale Meteorological Environment for Development of Tropical Cyclone Over North Atlantic Ocean Basin, J. Geophys. Res.-Atmos., 125, e2020JD033454, https://doi.org/10.1029/2020JD033454, 2020.

Tamarin-Brodsky, T. and Kaspi, Y.: Enhanced poleward propagation of storms under climate change, Nat. Geosci., 10, 908–913, https://doi.org/10.1038/s41561-017-0001-8, 2017.

Tang, Y., Han, Y., Ma, X., and Liu, Z.: Elevated heat pump effects of dust aerosol over Northwestern China during summer, Atmos. Res., 203, 95–104, https://doi.org/10.1016/j.atmosres.2017.12.004, 2018.

Tian, P., Zhang, L., Ma, J., Tang, K., Xu, L., Wang, Y., Cao, X., Liang, J., Ji, Y., Jiang, J. H., Yung, Y. L., and Zhang, R.: Radiative absorption enhancement of dust mixed with anthropogenic pollution over East Asia, Atmos. Chem. Phys., 18, 7815–7825, https://doi.org/10.5194/acp-18-7815-2018, 2018.

Trenberth, K. E. and Stepaniak, D. P.: Covariability of Components of Poleward Atmospheric Energy Transports on Seasonal and Interannual Timescales, J. Climate, 16, 3691–3705, https://doi.org/10.1175/1520-0442(2003)016<3691:COCOPA>2.0.CO;2, 2003.

University Corporation for Atmospheric Research (UCAR): WRF Source Codes and Graphics Software Downloads, UCAR [code], https://www2.mmm.ucar.edu/wrf/users/download/get_source.html, last access: 1 May 2026.

Uno, I., Eguchi, K., Yumimoto, K., Takemura, T., Shimizu, A., Uematsu, M., Liu, Z., Wang, Z., Hara, Y., and Sugimoto, N.: Asian dust transported one full circuit around the globe, Nat. Geosci., 2, 557–560, https://doi.org/10.1038/ngeo583, 2009.

Voss, K. K. and Evan, A. T.: A New Satellite-Based Global Climatology of Dust Aerosol Optical Depth, J. Appl. Meteorol. Clim., 59, 83–102, https://doi.org/10.1175/JAMC-D-19-0194.1, 2020.

Wang, M., Lau, W. K. M., and Wang, J.: Impact of middle east dust on subseasonal-to-seasonal variability of the Asian summer monsoon, Clim. Dynam., 58, 2041–2057, https://doi.org/10.1007/s00382-021-05694-z, 2021.

Wang, Y., Jiang, J. H., and Su, H.: Atmospheric responses to the redistribution of anthropogenic aerosols, J. Geophys. Res.-Atmos., 120, 9625–9641, https://doi.org/10.1002/2015JD023665, 2015.

Wang, Y., Zhang, R., and Saravanan, R.: Asian pollution climatically modulates mid-latitude cyclones following hierarchical modelling and observational analysis, Nat. Commun., 5, 3098, https://doi.org/10.1038/ncomms4098, 2014a.

Wang, Y., Wang, M., Zhang, R., Ghan, S. J., Lin, Y., Hu, J., Pan, B., Levy, M., Jiang, J. H., and Molina, M. J.: Assessing the effects of anthropogenic aerosols on Pacific storm track using a multiscale global climate model, P. Natl. Acad. Sci. USA, 111, 6894–6899, https://doi.org/10.1073/pnas.1403364111, 2014b.

Wang, Z., Huang, X., Wang, N., Xu, J., and Ding, A.: Aerosol-Radiation Interactions of Dust Storm Deteriorate Particle and Ozone Pollution in East China, J. Geophys. Res.-Atmos., 125, e2020JD033601, https://doi.org/10.1029/2020JD033601, 2020.

Xian, P., Klotzbach, P. J., Dunion, J. P., Janiga, M. A., Reid, J. S., Colarco, P. R., and Kipling, Z.: Revisiting the relationship between Atlantic dust and tropical cyclone activity using aerosol optical depth reanalyses: 2003–2018, Atmos. Chem. Phys., 20, 15357–15378, https://doi.org/10.5194/acp-20-15357-2020, 2020.

Xie, P. and Arkin, P. A.: Global Precipitation: A 17-Year Monthly Analysis Based on Gauge Observations, Satellite Estimates, and Numerical Model Outputs, B. Am. Meteorol. Soc., 78, 2539–2558, https://doi.org/10.1175/1520-0477(1997)078<2539:GPAYMA>2.0.CO;2, 1997.

Xu, H., Guo, J., Wang, Y., Zhao, C., Zhang, Z., Min, M., Miao, Y., Liu, H., He, J., Zhou, S., and Zhai, P.: Warming effect of dust aerosols modulated by overlapping clouds below, Atmos. Environ., 166, 393–402, https://doi.org/10.1016/j.atmosenv.2017.07.036, 2017.

Yin, Z., Wan, Y., Zhang, Y., and Wang, H.: Why super sandstorm 2021 in North China?, Natl. Sci. Rev., 9, nwab165, https://doi.org/10.1093/nsr/nwab165, 2022.

Yin, Z., Huo, Q., Hu, D., Huang, Y., and Wang, H.: Why record-breaking gale and nationwide dust in China in April 2025, Sci. Bull., 71, 463–465, https://doi.org/10.1016/j.scib.2025.11.054, 2026.

Yu, Y., Kalashnikova, O. V., Garay, M. J., and Notaro, M.: Climatology of Asian dust activation and transport potential based on MISR satellite observations and trajectory analysis, Atmos. Chem. Phys., 19, 363–378, https://doi.org/10.5194/acp-19-363-2019, 2019.

Yuan, Y., Wang, H., Wu, C., Hu, T., Wu, F., Zhang, D., and Cao, J.: Weaker absorption of Asian dust than previously estimated based on observation-constrained simulation, npj Clim. Atmos. Sci., 9, 19, https://doi.org/10.1038/s41612-025-01290-8, 2026.

Zeng, Y., Wang, M., Zhao, C., Zhu, Y., Rosenfeld, D., and Huang, K.-E.: Extremely High Concentrations of Ice Particles in East Asian Dust-Infused Baroclinic Storm (DIBS) Cirrus Shield: Dominant Role of Dust Ice Nucleation Effect, J. Geophys. Res.-Atmos., 128, e2022JD038034, https://doi.org/10.1029/2022JD038034, 2023.

Zhang, R., Li, G., Fan, J., Wu, D. L., and Molina, M. J.: Intensification of Pacific storm track linked to Asian pollution, P. Natl. Acad. Sci. USA, 104, 5295–5299, https://doi.org/10.1073/pnas.0700618104, 2007.

Zhang, X., Li, L., Che, H., Dubovik, O., Derimian, Y., Holben, B., Gupta, P., Eck, T. F., Lind, E. S., Toledano, C., Xia, X., Zheng, Y., Gui, K., and Zhang, X.: Aerosol Components Derived from Global AERONET Measurements by GRASP: A New Value-Added Aerosol Component Global Dataset and Its Application, B. Am. Meteorol. Soc., 105, E1822–E1848, https://doi.org/10.1175/BAMS-D-23-0260.1, 2024.

Zhao, C., Liu, X., and Leung, L. R.: Impact of the Desert dust on the summer monsoon system over Southwestern North America, Atmos. Chem. Phys., 12, 3717-3731, https://doi.org/10.5194/acp-12-3717-2012, 2012.

Zhao, J., Ma, X., Wu, S., and Sha, T.: Dust emission and transport in Northwest China: WRF-Chem simulation and comparisons with multi-sensor observations, Atmos. Res., 241, 104978, https://doi.org/10.1016/j.atmosres.2020.104978, 2020.

Zhou, R. and Deng, Y.: A model analysis of the interactions between East Asian anthropogenic aerosols and North Pacific atmospheric transients in boreal winter, J. Geophys. Res.-Atmos., 118, 306–316, https://doi.org/10.1029/2012JD018649, 2013.

Zhou, T., Zhou, X., Yang, Z., Córdoba-Jabonero, C., Wang, Y., Huang, Z., Da, P., Luo, Q., Zhang, Z., Shi, J., Bi, J., and Alikhodja, H.: Transboundary transport of non-east and East Asian dust observed at Dunhuang, northwest China, Atmos. Environ., 318, 120197, https://doi.org/10.1016/j.atmosenv.2023.120197, 2024.

Zhu, A., Ramanathan, V., Li, F., and Kim, D.: Dust plumes over the Pacific, Indian, and Atlantic oceans: Climatology and radiative impact, J. Geophys. Res.-Atmos., 112, D16208, https://doi.org/10.1029/2007JD008427, 2007.

Zhu, A., Xu, H., Deng, J., Ma, J., and Li, S.: El Niño–Southern Oscillation (ENSO) effect on interannual variability in spring aerosols over East Asia, Atmos. Chem. Phys., 21, 5919–5933, https://doi.org/10.5194/acp-21-5919-2021, 2021.